TRANSITION METAL DIMERS ON GAAS(110) SURFACE: A DFT STUDY

A THESIS SUBMITTED TO
THE GRADUATE SCHOOL OF ENGINEERING AND SCIENCE
OF BILKENT UNIVERSITY
IN PARTIAL FULFILLMENT OF THE REQUIREMENTS FOR
THE DEGREE OF
MASTER OF SCIENCE
IN
MATERIALS SCIENCE AND NANOTECHNOLOGY

By
Ahmet Alaybeyoğlu
January 2025

Transition Metal Dimers on GaAs(110) Surface: A DFT study
By Ahmet Alaybeyoğlu
January 2025

We certify that we have read this thesis and that in our opinion it is fully adequate, in scope and in quality, as a thesis for the degree of Master of Science.

Cüneyt Şahin(Advisor)

Engin Durgun

Aybey Moğulkoç

Approved for the Graduate School of Engineering and Science:

Orhan Arıkan
Director of the Graduate School

ABSTRACT

TRANSITION METAL DIMERS ON GAAS(110) SURFACE: A DFT STUDY

Ahmet Alaybeyoğlu
M.S. in MATERIALS SCIENCE AND NANOTECHNOLOGY
Advisor: Cüneyt Şahin
January 2025

Dilute magnetic semiconductors (DMSs) have gained appreciable interest in the past two decades. This is due to the perspectives of both fundamental physics and novel applications. They are useful in the context of single dopants (solotronics) because studying individual dopants and their interactions with the host provides rich physics. Here we carry out density functional theory calculations for transition metal element dimer dopants on GaAs(110) surface using Quantum Espresso software by employing ultra-soft pseudopotentials (USPP) and report properties such as exchange energy, spin-resolved density of states, spin-resolved projected density of states, structural and magnetic relaxations, and STM images of surface with dimers. We model the GaAs(110) surface with the BURAI software package, and we study 4 transition metal dimers on near and far configurations on the surface, Fe, Cr, V, and Co. Since the dopants are magnetic, we consider both the ferromagnetic and antiferromagnetic alignments. We show that magnetic configurations greatly alter the relaxed positions of dopants. We also report the exchange energy between ferromagnetic (triplet) and antiferromagnetic (singlet) states for near and far configurations. At the end of our calculations, we found the relationship between exchange energy and distance and reported a dramatic change in the magnitude of the exchange energy as a function of dimer separation. We also observe that except for the Co dimers, Fe, Cr, and V dimers have a reasonable exchange energy between ferromagnetic and antiferromagnetic alignments. This is due to nonzero magnetic moments on these transition metal dopants. For less than two percent of dopant ratio, we observed a metallic system for Fe dimer, a semiconducting system for Cr, and a half-metallic system for V dimers. Electronic structure calculations such as DOS and PDOS projections are in parallel with the expectations of ferromagnetic and antiferromagnetic alignments. We also study scanning tunneling microscopic images of these dimers on the surface showing a large contrast under a bias voltage of 1V. Semiconducting

surfaces such as GaAs hosting transition metal dopants with d-orbitals in this thesis have the potential to be excellent platforms for novel quantum applications such as fast-switching qubits. Also, reported spin-resolved density of states (DOS) and spin-resolved projected density of states can be used to understand the hybridization of bands, exchange splitting on orbitals, and design materials for future spintronic and optical applications.

Keywords: Density Functional Theory (DFT), Transition Metal Dopants, Dimer, GaAs(110) surface, Exchange Energy, Scanning Tunneling Microscope, Ferromagnetism, Antiferromagnetism.

ÖZET

GAAS(110) YÜZEYİ ÜZERİNDE GEÇİŞ METALİ DİMERLER: BİR YOG̃UNLUK FONKSİYONELİ (DFT) ÇALIŞMASI

Ahmet Alaybeyoğlu
Malzeme Bilimi ve Nanoteknoloji, Yüksek Lisans
Tez Danışmanı: Cüneyt Şahin
Ocak 2025

Son yirmi yılda, seyreltilmiş manyetik yarıiletkenler (DMS'ler), hem temel fizik hem de yenilikçi uygulamalar açısından büyük ilgi görmüştür. Özellikle, tekil katkılayıcıların ve bunların ana malzeme ile etkileşimlerinin incelenmesi, solotronik olarak bilinen tekil katkılayıcılar bağlamında zengin fiziksel bilgiler sunmaktadır. Bu çalışmada, geçiş metali elementi dimer katkılayıcılarının GaAs(110) yüzeyindeki özelliklerini incelemek için Quantum Espresso yazılımını kullanarak yoğunluk fonksiyoneli teorisi (DFT) hesaplamaları gerçekleştirdik. Bu hesaplamalarda ultra-yumuşak pseudopotansiyeller (USPP) kullanılmıştır ve değişim enerjisi, spin-çözünür yoğunluk durumu (DOS), spin-çözünür projeksiyonlu yoğunluk durumu (PDOS), yapısal ve manyetik rahatlamalar ile dimerlerin bulunduğu yüzeyin taramalı tünelleme mikroskobu (STM) görüntüleri gibi özellikler rapor edilmiştir. GaAs(110) yüzeyi BURAI yazılım paketi ile modellenmiş ve Fe, Cr, V ve Co olmak üzere dört farklı geçiş metali dimeri yüzey üzerindeki yakın ve uzak konfigürasyonlarda incelenmiştir. Katkılayıcılar manyetik özelliklere sahip olduğundan, hem ferromanyetik (triplet) hem de antiferromanyetik (singlet) hizalanmalar dikkate alınmıştır. Çalışmamız, manyetik konfigürasyonların katkılayıcıların rahatlamış pozisyonlarını büyük ölçüde değiştirdiğini göstermektedir. Ayrıca, yakın ve uzak konfigürasyonlar için ferromanyetik (triplet) ve antiferromanyetik (singlet) durumlar arasındaki değişim enerjisini rapor ettik. Hesaplamalarımız sonucunda, değişim enerjisi ile dimer ayrımı arasındaki ilişkiyi belirledik ve değişim enerjisinin büyüklüğünde dimer ayrımına bağlı olarak dramatik bir değişim gözlemledik. Çalışma sonuçlarımız, Co dimerleri dışında, Fe, Cr ve V dimerlerinin ferromanyetik (triplet) ve antiferromanyetik (singlet) hizalanmalar arasında makul bir değişim enerjisine sahip olduğunu göstermektedir. Bu durum, bu geçiş metali katkılayıcılarının sıfırdan farklı manyetik momentlere

sahip olmasından kaynaklanmaktadır. Yüzde iki oranından daha az katkılayıcı yoğunluğunda, Fe dimeri için metalik bir sistem, Cr dimeri için yarıiletken bir sistem ve V dimeri için yarı-metalik bir sistem gözlemlenmiştir. Elektronik yapı hesaplamaları (DOS ve PDOS projeksiyonları) ferromanyetik (triplet) ve antiferromanyetik (singlet) hizalanmaların beklentileriyle uyum içerisindedir. Ayrıca, bu dimerlerin yüzey üzerindeki taramalı tünelleme mikroskop (STM) görüntüleri incelenmiş ve 1 V öngerilim altında büyük bir kontrast gözlemlenmiştir.Bu tezde, GaAs gibi yarı iletken yüzeylerin d-orbitaline sahip geçiş metalleriyle katkılanmasıyla, hızlı anahtarlama yapabilen kübitler gibi yenilikçi kuantum uygulamaları için mükemmel platformlar olma potansiyeline sahip olduğu gösterilmiştir. Ayrıca, rapor edilen spin-çözünür yoğunluk durumu (DOS) ve spin-çözünür projeksiyonlu yoğunluk durumu (PDOS) hesaplamaları, bantların hibritleşmesi, orbitallerdeki değişim bölünmesi gibi fenomenleri anlamak ve gelecekteki spintronik ve optik uygulamalar için malzeme tasarımına katkıda bulunmak amacıyla kullanılabilir.

Anahtar sözcükler: Yoğunluk Fonsiyoneli (DFT), Geçiş Metali Katıklar, Dimer, GaAs(110) yüzeyi, Değişim Enerjisi, Taramalı Tünelleme Mikroskop (STM), Ferromanyetizma, Antiferromanyetizma.

Acknowledgement

I express my deepest gratitude to my advisor, Cüneyt Şahin, for his guidance and support throughout this work. I am grateful to my family for their love and encouragement, and to my friends for their support and understanding. This achievement would not have been possible without all of you.

Contents

List of Figures

List of Tables

Chapter 1

Introduction

1.1 Semiconductors and Single Dopants (Solotronics)

Within the scientific community, the interactions between dopants and semiconductor materials have long been a focal point of investigation. These studies have revealed a wide range of tunable phenomena, including dilute magnetic semiconductors (DMS) [2, 3] and single-photon sources [4, 5]. Recently, a key objective in semiconductor research has been to reduce device dimensions. Theoretically, this miniaturization can extend to the limit of a single dopant, reflecting the discrete nature of matter [6]. Traditionally, the collective behavior of dopant ensembles dominated our understanding of semiconductor properties. However, recent advancements have shifted focus to the properties of individual dopants, a field now known as solotronics. This paradigm shift has opened new avenues for studying the fundamental characteristics of single dopants, which have been explored extensively across a wide range of materials and applications [7, 8, 9, 10, 11, 12, 13]. For practical applications, epitaxial beam growth techniques have played a crucial role in advancing solotronic device fabrication [14]. As devices continue to shrink, the bulk-to-surface ratio increases and results in significant changes to the device

geometry. Impurities that previously resided in the bulk are more likely to be located near or on surfaces, where quantum confinement and surface effects can profoundly alter device characteristics [15]. This shift in behavior motivates us to study the intricate interplay between single dopants and their semiconductor environments. By understanding these effects, we aim to uncover new opportunities for innovation in solotronic devices and their commercial applications.

The interaction of an impurity with its surroundings determines how it can be manipulated and sensed. While the host crystal forms the primary environment, other factors such as nearby impurities, electric and magnetic fields, confinement potentials, photons, and phonons also contribute. To utilize single impurities in active devices, their states must be altered through externally controlled environments. The most straightforward operation involves gate-induced impurity ionization, a principle underlying most electronic devices. An electric field from a gate electrode ionizes a dopant atom, impurity, or quantum dot within a semiconductor, modifying its charge state by releasing or capturing electrons. Achieving single-impurity ionization requires either a nanoscale gate or a low impurity density. The former was shown by ionizing single impurities with an STM [16], and used for measurement of the binding energy of an electron to a Si donor at the GaAs-vacuum contact [17]. While ionization is the most apparent outcome of an impurity's interaction with an electric field, subtler effects such as changes in binding energy and wavefunction precede it. Additionally, strain—though not easily subject to active manipulation—significantly influences the impurity environment. Experimental studies have investigated impurities near strained self-assembled quantum dots [18] or surface reconstructions [19]. These studies reveal that strain, resulting from surface reconstruction, plays a crucial role in determining the behavior of impurities beneath reconstructed surfaces [20, 21, 22]. This insight underscores the importance of relaxation calculations in computational studies, allowing us to model and understand surface reconstructions accurately.

An exceptional type of impurity in solotronics is the nitrogen-vacancy (NV) center in bulk diamond. These centers introduce in-gap states due to defects, ensuring the absence of free carriers in the NV state. As a result, the defect properties dominate, making NV centers a widely studied model system

for exploring fundamental quantum-mechanical effects on individual impurities [23, 24, 25, 26, 27]. Advanced optical techniques have been developed to assess individual impurities in single NV centers, such as confocal microscopy [28] and stimulated depletion microscopy [29]. An example figure is shown in Figure **??**. NV centers are produced by replacing one C atom in a diamond where it sits behind a vacancy.

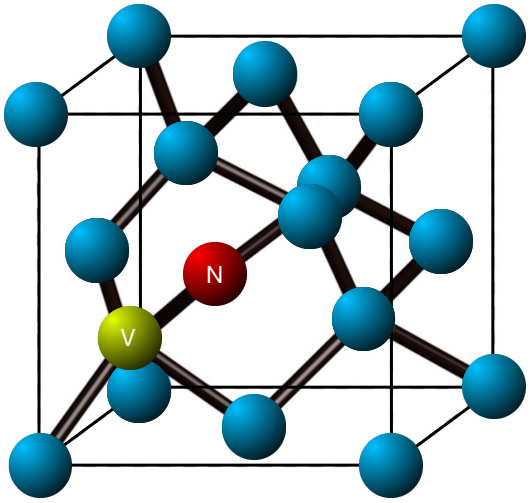

Figure 1.1: NV center in a diamond. Blue atoms are C, the red atom is N, and the vacancy of the C atom is shown with V. (Reproduced from Ref. [1])

Another important system is quantum dots, which serve as a platform for studying single electrons in semiconductors. While quantum dots offer several advantages—particularly in applications where gate control is crucial—they also present challenges such as reproducibility issues and the limited feasibility of all-optical techniques. These limitations have shifted research interest toward impurities like NV centers, which exhibit more robust and reproducible behavior under optical and quantum manipulation.

The construction of heterogeneous impurity molecules, composed of various impurity species arranged in artificial patterns, opens a vast landscape of possibilities. This emerging field of molecular impurity physics holds as many opportunities as traditional chemistry, potentially revolutionizing how we understand and manipulate material properties. The formation of heterogeneous impurity

molecules on the GaAs surface [30] marks a promising step toward advancements in atomic-scale control of spin-spin interactions. The scanning tunneling microscope (STM) has demonstrated remarkable capability in the artificial arrangement of impurities in semiconductors, approaching the precision of atom manipulation achieved on metal surfaces. However, an even more elegant approach would involve leveraging spontaneous self-assembly processes to create such structures naturally. Additionally, exploring bistable and mobile impurities could enable the development of more complex functionalities, further expanding the potential of this field.

1.2 Experimental Techniques

Three related techniques essential to investigating and manipulating material surfaces, especially semiconductors, are ion implantation, scanning tunneling microscopy (STM), and spin-polarized scanning tunneling microscopy (SP-STM). Cross-sectional STM (XSTM) complements these techniques by examining cleaved surfaces, revealing subsurface structures and interface characteristics crucial for device integration and performance.

By exposing the surface to high-energy ions, ion implantation modifies materials' structural, electrical, and magnetic characteristics by introducing dopants. These changes are essential to customizing semiconductor surfaces, like GaAs(110). These surfaces can be seen at the atomic scale using STM, which makes it possible to identify topographic and electronic state changes brought on by ion implantation. The local density of states is directly reflected in the tunneling current in STM, providing information about the effects of implantation-induced defects on surface characteristics. By adding a spin-polarized tip, SP-STM expands on the capabilities of STM and enables the investigation of magnetic characteristics at the atomic level. This is particularly important for materials where spin-dependent electronic structures or magnetic characteristics are altered by ion implantation. Combined, these methods offer a thorough comprehension of surface phenomena, including structural, electrical, and magnetic

viewpoints crucial for advancing the study of atomic-scale devices.

The most advanced approach for studying impurities on III-V semiconductors is STM and XSTM. One important note on the XSTM approach, it is primarily restricted to the III-V and II-VI semiconductor materials' natural (110) cleavage plane. Wavefunction imaging, the ability to manipulate charges, and the possibility of combining electric, magnetic, and optical analysis are three domains in which the STM technology excels. STM still faces significant difficulties in obtaining magnetic information, such as spin detection, on a single impurity; nonetheless, the first successful investigation of a magnetic Fe impurity on a surface layer of InSb was published [31]. About a decade ago, STM-induced substitution of Mn, Fe, and Co in a GaAs(110) surface layer showed nearly atomic resolution in single-impurity implantation [32, 33].

Magnetic-field-dependent ESR technique used in single impurities as well [34]. It is important because the spin information gathered could solve the problem of determining the impurity's chemical nature under the scanning tip, which is one of the outstanding problems we face today. This technique yields clear results of donors on GaAs for Si [35], and Zn [36] acceptors. Proposed methods to control a single spin in a solid state environment depend on magnetic resonance [37, 38] or optical manipulation [39, 40, 41]. There has been development toward substituting the spin-orbit interaction [42, 43] or the exchange interaction [44, 45] for magnetic control.

1.3 Spintronics and Quantum Computing

The miniaturization of semiconductors advances, but the obstacle related to tunneling effects at the atomic scale and eager to advance the power consumption and performance of the devices, researchers are working on implementing spin degree of freedom into the semiconductor devices. In read heads of HDDs, the spin degree of freedom is introduced to the electronics by GMR [46, 47]. This relatively new field called spintronics has gained appreciable interest due to its

importance for possible applications in memories [48, 49, 50, 51], magnetic sensors, radio frequency and microwave devices, logic and non-Boolean devices in the microelectronic industry [52].

About 20 years ago, single impurities were proposed to be used in quantum computing as 'qubits'. Such proposals are made on using nuclear spin, [38] single dopant's bound electron spin [53], and bound electron charge [54]. According to an estimation [55], quantum computers can outperform classical computers if they can reach 10^6 qubits with 10^{-6} probability in each operation. Following Kane's nuclear spin-based quantum computer paper [38], two critical insights with the realization of quantum computers are proposed. First, the algorithms quantum computers will use can reach a much higher speed than conventional computers [56, 57, 58], and second, error-correcting codes are developed to eliminate disturbances from surrounding [59, 60]. From the perspective of quantum processing, identifying methods to couple local electric fields to the spin properties of an impurity is highly beneficial. In a semiconductor, an alternating current electric field applied to a single donor-bound electron modifies the orbital features of its wave function, which in turn affects the spin dynamics of the electron via the spin-orbit interaction. A definitive plan proposed [61] for the electrical initialization, manipulation, and detection of individual pseudospin states of a magnetic dopant within a semiconductor. When the ground state possesses a nonzero integer spin, it is feasible to execute all necessary spin operations solely by applying electric fields thus may offer a pathway to high-density, scalable spin-based devices. It should be feasible to achieve all-electrical spin manipulation for various impurities in tetrahedral semiconductors that exhibit $J > \frac{1}{2}$ ground state spins, such as the majority of transition-metal ions in these semiconductors or the nitrogen-vacancy center present in diamond. Also, a novel all-electrical approach was proposed for manipulating ionic spins, substituting the conventional magnetic fields used in electron spin resonance (ESR) with electric fields [62]. We suggest the exchange energy between ferromagnetic (triplet) and antiferromagnetic (singlet) states could be used in quantum computing as fast-switching qubits [45].

1.4 Diluted Magnetic Semiconductors (DMSs)

Spintronics applications have not been limited to the write heads of hard drives. Researchers have actively worked on introducing magnetism into semiconductors by incorporating transition metal elements, creating a class of materials known as dilute magnetic semiconductors (DMSs). These semiconductors have been classified as paramagnetic or ferromagnetic based on their final magnetic configuration. Paramagnetic DMSs have typically been based on II-VI materials with a small percentage of manganese (Mn) [63]. In these materials, carriers have become spin-polarized due to giant Zeeman splitting caused by non-interacting Mn ions. Paramagnetic DMSs have exhibited either p-type or n-type behavior. Researchers have successfully demonstrated spin injection applications [64] and voltage-controlled spin valves [65]. However, the primary limitation of paramagnetic DMSs has been their volatility. These materials have consistently lost spin information in the absence of an external magnetic field, rendering them unsuitable for applications like magnetic random-access memory (MRAM), which has required non-volatile materials.

The discovery of ferromagnetism in p-type Mn-doped IV-VI semiconductors has been investigated in [66], for III-V semiconductors in [67, 68, 69], and for II-VI semiconductors in [70, 71]. Ferromagnetic-type semiconductors have been identified as nonvolatile, making them suitable candidates for MRAM-based applications. One important finding has been that all ferromagnetic semiconductors have consistently exhibited p-type behavior. Because most ferromagnetic semiconductors have been doped with Mn, the coupling between electrons and Mn ions has proven much weaker than the coupling between holes and Mn ions due to p-d exchange [63]. The exclusive presence of p-type semiconductors has implied that only hole transport has been possible, resulting in much shorter spin coherence compared to electron transport. The most significant drawback of dilute magnetic semiconductors has been that their Curie temperatures remain well below room temperature.

GaAs has become an attractive DMS since the 1990s and mid-2010s due to

Mn doping. In 1996, Ohno et al. have demonstrated in-plane ferromagnetic order in MBE-grown Mn-doped GaAs films at a Curie temperature of 60 K [68]. By 1998, a higher Curie temperature of 110 K has been achieved by Matsukura et al. [65]. In 2011, a Curie temperature of 200 K has been reported for heavily Mn-doped (Ga, Mn)As films (16.2% Mn) shaped into nanowires [72]. However, due to strong antiferromagnetic coupling between Mn ions and neighboring substitutional atoms, the antiferromagnetic superexchange interaction and the ferromagnetic double exchange interactions have competed, preventing arbitrary tuning of Mn concentration [73]. To enhance ferromagnetism in dilute magnetic semiconductors, co-doping has been proposed [74]. Ab initio calculations have been conducted on the GaAs(110) surface for single and paired Mn surface atom substitution [75]. Additionally, the GaAs(110) surface has been studied for different dopants. Single-Co [76] and single-Fe [77] impurities have been investigated using DFT; however, studies on dimers and exchange energy between them have remained absent.

1.5 GaAs as a Host Material

We have discussed the general structure of semiconductors and defects; now we move on to selecting a suitable host semiconductor, and then we will explore the different defects in the chosen host semiconductor. The choice of a host material in DMS plays a critical role in shaping the fundamental properties of the resultant material because the host material greatly influences the resultant DMS. Some of the most widely studied host materials for DMS are GaAs, InSb, GaN, ZnO, and CdTe. Among these five, (Ga,Mn)As is the most widely studied DMS.

Our host material is GaAs. Optical spectroscopy on GaAs samples for single impurity centers is conducted in a luminescence study of individual isoelectronic N-pairs [78]. In one study with GaAs quantum wells, a single impurity plays a role in a double-barrier resonant-tunneling (DBRT) [79]. Another study uses GaAs quantum wells to isolate Mn acceptors in an environment where the thermal energy is less than the bandgap of GaAs [80].

Gallium arsenide (GaAs) is the second most commonly used semiconductor, especially in optoelectronic and high-frequency applications, and is studied as a host material in various contexts for exploring different phenomena to yield a helpful device or to understand semiconductor physics better. It is an III-V direct band gap semiconductor with a zinc-blende crystal structure. It is used in microwave frequency integrated circuits, infrared light-emitting diodes, laser diodes, and solar cells. Each arsenic atom has four gallium nearest neighbors, and each gallium atom has four arsenic nearest neighbors arranged in a tetrahedral structure. The dimension of the conventional unit cell is 0.565325 nm at room temperature, and this semiconductor's density is $5.32\,\mathrm{g\,cm^{-3}}$ [81].

For electrons in gallium arsenide (GaAs), the steady-state drift velocity vs. electric field relation shows a high mobility of about $8000\,\mathrm{cm^2\,V^{-1}\,s^{-1}}$ at moderate fields. GaAs' low-field hole mobility is about $400\,\mathrm{cm^2\,V^{-1}\,s^{-1}}$, making it suitable for many electrical devices, especially those relying on electron transport. Both doping and compensation ratios strongly influence the mobility of carriers in GaAs. However, the low thermal conductivity of GaAs is $0.46\,\mathrm{W\,cm^{-1}\,^\circ C}$, at $300\,\mathrm{K}$ makes it less desirable for device applications compared to silicon.

GaAs, a lattice-matched to (Ga,Al)As, find wide-ranging uses in the technology of optical devices, encompassing photodiodes, solar cells, lasers, and LEDs. Its optical characteristics are fascinating because it exhibits the distinct absorption edge of a direct gap semiconductor. Exciton absorption causes a peak in the absorption spectra to appear near the fundamental absorption edge at low temperatures. Because of band tailing and exciton screening, the absorption edge of extensively doped GaAs is wider, which reduces exciton absorption near the band edge. At wavelengths longer than approximately $4\,\mu\mathrm{m}$, the absorption coefficient rises due to free electron absorption. Absorption is dominated by optically aided transitions at wavelengths shorter than the bandgap. GaAs has a static dielectric constant that varies with temperature and frequency, with a static dielectric constant of $\kappa_0 = 12.40$ and a high-frequency dielectric constant of $\kappa_\infty = 10.60$ [81].

1.6 This thesis

After reviewing the literature in Chapter 1, in Chapter 2 we discuss the exchange energy and an overview of DFT. Chapter 3 is devoted to methods where we describe the modeling of the system and convergence tests. Later on in the same chapter, we show our calculations, such as structural relaxations of GaAs(110) surface with and without defects, exchange energy between transition metal pairs, and magnetic moments. We also calculate the total and projected density of states to examine the contribution of defects, especially to the states around the Fermi level in Chapter 3. Additionally, in Chapter 3, we report the calculations of scanning tunneling images of the dimers on the GaAs surface. In Chapter 4, we end this dissertation with a conclusion, including a summary of this work and future directions that can be taken.

Chapter 2

Theory

The rapidly developing interdisciplinary area of computational materials science uses different computational methods to analyze, design, and predict the atomic and molecular-level characteristics and behavior of materials. Computational materials science is essential for solving difficult problems in material design, characterization, and optimization because of its capacity to simulate and model the fundamental interactions that exist within materials. Density Functional Theory (DFT), a quantum mechanical approach that offers a powerful tool for resolving the many-body problem that emerges in the study of interacting electrons in materials, is the foundation of many computational approaches employed in this field.

The many-body problem refers to the challenge of describing systems with a large number of interacting particles, such as electrons in a solid. This problem is inherently complex due to the nonlinear interactions between particles, making exact solutions for large systems computationally intractable. By concentrating on the electron density instead of the many-body wavefunction, DFT offers an effective approximation that significantly reduces the complexity of the problem while maintaining accurate calculations for a variety of materials. DFT calculations can be broadly classified into various types depending on the level of approximations such as the treatment of core electrons, employed basis set, and

exchange-correlation (XC) potential. In all-electron calculations for core electrons, the interactions of all electrons, including core and valence electrons, are treated explicitly. These calculations offer high accuracy, but can be computationally expensive, especially for larger systems. By substituting an effective potential for core electrons, pseudopotential approaches, on the other hand, simplify the treatment of core electrons and enable the precise description of valence electrons at a lower computing cost.

Basis sets define the mathematical representation of electronic wavefunctions. Plane-wave basis sets are well-suited for periodic systems due to their systematic convergence and give overall good accuracy results in a reasonable accuracy. In contrast, atom-centered basis sets are better at describing isolated systems and localized states, means higher accuracy, but they are slower. Lastly, XC functionals play a central role in capturing quantum mechanical exchange and correlation effects. The Local Density Approximation (LDA) is computationally efficient and reliable for uniform systems, making it effective for studying magnetic and structural properties. For this thesis, LDA is employed due to its robustness in capturing magnetic interactions, structural and electronic features relevant to the studied systems.

Excellent books written for studying DFT in detail [82, 83, 84], that's why we will not provide details about density functional theory which is based on works of Hohenberg, Kohn, and Sham [85, 86]. Since then, DFT has been improved by many scientists to include effects such as relativistic correction to study magnetic materials and spin-orbit coupling [87, 88], improving the accuracy by approximations such as LDA and GGA [89, 90], and introducing time-dependent density functional theory for studying excited state properties [91].

Now we will briefly explain the magnetism in a quantum mechanical manner [92]. Solution of Dirac's equation yields 4 quantum numbers; n, l, m_l, and s. Magnetism occurs as a result of the total angular momentum of the electrons which consist of orbital angular momentum due to negatively charged electrons orbiting around the positively charged nuclei (l) and the intrinsic angular momentum called spin (s). The collective interaction between total angular moments

in a material is responsible for the magnetism. The strength of such interaction can be modeled easily using Heisenberg's Hamiltonian with the exchange interaction which is the main explanation of the local moment theory. In general, two theories used to explain the intriguing phenomenon of magnetism, are local moment and collective electron theories. However, in this thesis we will concentrate on the calculation of the exchange coupling J that is inherently responsible for magnetism in DMS systems.

2.1 Exchange Interaction

Exchange interaction is a quantum mechanical property for the states of indistinguishable particles. Indistinguishable particles sometimes called identical particles can be either bosons or fermions. The main difference between the fermions and bosons is the exchange symmetry. This property alters the expectation value of the particles oppositely. Bosons have symmetric total wavefunctions, namely, when the two bosons are exchanged, the total wave function stays the same. However fermions have antisymmetric wavefunctions, as a result the wavefunction changes its sign when we interchange their positions [93, 94, 95]. The best way to understand the phenomenon called exchange we consider two Hydrogen atoms with two electrons: The wavefunction for these electrons:

$$\psi(x_1, x_2) = \psi_a(x_1)\psi_b(x_2) \tag{2.1}$$

The total wavefunction of such a system can be written in two different ways with two distinc symmetries as explaine above:

$$\psi_+(x_1, x_2) = \frac{1}{\sqrt{2}}[\psi_a(x_1)\psi_b(x_2) + \psi_b(x_1)\psi_a(x_2)] \tag{2.2}$$

for symmetric wavefunctions (bosons), and,

$$\psi_-(x_1, x_2) = \frac{1}{\sqrt{2}}[\psi_a(x_1)\psi_b(x_2) - \psi_b(x_1)\psi_a(x_2)] \tag{2.3}$$

for antisymmetric wavefunctions (fermions). We also normalized them with ($\frac{1}{\sqrt{2}}$). ψ_a and ψ_b are the two different states, given in two different positions x_1 and x_2. In that case $\psi_+(x_1, x_2)$ corresponds to boson (symmetric wavefunction) and $\psi_-(x_1, x_2)$ is fermion (antisymmetric wavefunction).

In order to see so called exchange force we need to calculate the expectation values of the average distance between them. The expectation value of average distance between two positions is denoted by subscript d, and subscripts a and b are for two different states. The expectation value of the square of the separation distance between the two particles calculated as following:

$$\langle (x_1 - x_2)^2 \rangle_d = \langle x^2 \rangle_a + \langle x^2 \rangle_b - 2\langle x \rangle_a \langle x \rangle_b \tag{2.4}$$

where,

$$\langle x^2 \rangle_i = \int dx\, x^2 |\psi_i(x_1)|^2 \tag{2.5}$$

ends up with,

$$\langle (x_1 - x_2)^2 \rangle_\pm = \langle (x_1 - x_2)^2 \rangle_d \mp 2\langle x_2 \rangle_{ab} \tag{2.6}$$

where ,

$$\langle x \rangle_{ab} = \int dx\, x\, \psi_a^*(x) \psi_b(x) \tag{2.7}$$

Due to symmetry constarints on wavefunction of bosons and fermions, which upper sign for bosons and lower sign for fermions, bosons tend to be closer together and fermions farther from each other. Thus we name it a force of attraction between bosons, and force of repulsion between fermions, namely the exchange force as shown in Figure 2.1.

Considering the Dirac's equation for more accurate picture of the reality, now

Figure 2.1: Exchange force. (a) represents boson and (b) represents fermion.

we are including the spin to the system which can be only up or down for stationary state picture. Now we are writing the total wave function of the system for two electrons given where ψ will correponds the spatial part and ϕ is the spin part.

$$\psi_{tot}(x_1, x_2, s_1, s_2) = \psi(x_1, x_2)\phi(s_1, s_2) \tag{2.8}$$

Since the calculating symmetric and antisymmetric configurations for spatial part is tidious we will look at the spin part only. Two important thing to note in possible spin parts, first we can not distinguish electrons, second it has to be anti-symmetric for symmetric spatial part and symmetric for anti-symmetric spatial part due to fact that electrons are fermion. We will classify them into two categories as singlet and triplet states. Singlet state with total spin S=0 where the two spin are anti parallel (thus antisymmetric) and triplet state with total spin S=1 is when they are in parallel alignment (thus symmetric). By looking at this states we will comment about the characteristics of the system as ferromagnetic or antiferromagnetic.

$$|\psi_{\text{singlet}}\rangle = \frac{1}{\sqrt{2}}\left(|\uparrow\downarrow\rangle - |\downarrow\uparrow\rangle\right) \tag{2.9}$$

$$|\psi_{\text{triplet}}\rangle = \begin{cases} |\psi_{+1}\rangle = |\uparrow\uparrow\rangle & \text{for } S_z = +1 \\ |\psi_0\rangle = \frac{1}{\sqrt{2}}\left(|\uparrow\downarrow\rangle + |\downarrow\uparrow\rangle\right) & \text{for } S_z = 0 \\ |\psi_{-1}\rangle = |\downarrow\downarrow\rangle & \text{for } S_z = -1 \end{cases} \tag{2.10}$$

Following the book [92], we will describe the simplest many-body Hamiltonian

which would consist of two idealized hydrogen atoms. First, we construct the total Hamiltonian by considering the Coulomb interaction.

$$H = H_1 + H_2 + H_{12} \tag{2.11}$$

and each part of the Hamiltonian is given by:

$$H_1 = -\frac{h^2}{2m_e}\nabla_1^2 - \frac{Ze^2}{4\pi\epsilon_0 r_1}, \tag{2.12}$$

$$H_2 = -\frac{h^2}{2m_e}\nabla_2^2 - \frac{Ze^2}{4\pi\epsilon_0 r_2}, \tag{2.13}$$

$$H_{12} = \frac{e^2}{4\pi\epsilon_0 r_{12}} \tag{2.14}$$

The first two terms correspond to the kinetic energy of the electron in H_1 and H_2. The second term in these two Hamiltonian is the potential energy due to Coulomb interaction between the nuclei and the electron. In the last term, H_{12} potential energy occurring from electron-electron interaction through Coulomb potential is represented. The expectation value of the Hamiltonian will give us the total energy.

$$\begin{aligned} E &= \langle\psi(r_1, r_2)|H|\psi(r_1, r_2)\rangle \\ &= \frac{1}{2}\langle[\phi_1(r_1)\phi_2(r_2) \pm \phi_2(r_1)\phi_2(r_2)]| \\ &\quad (H_1 + H_2 + H_{12})|[\phi_1(r_1)\phi_2(r_2) \pm \phi_2(r_1)\phi_1(r_2)]\rangle \end{aligned} \tag{2.15}$$

Carrying out the matrix multiplication results in:

$$
\begin{aligned}
E = \frac{1}{2}\Big[&\langle\phi_1(r_1)|H_1|\phi_1(r_1)\rangle + \langle\phi_2(r_1)|H_1|\phi_2(r_1)\rangle \\
&+ \langle\phi_1(r_2)|H_2|\phi_1(r_2)\rangle + \langle\phi_{2s}(r_2)|H_2|\phi_2(r_2)\rangle \\
&+ \langle\phi_1(r_1)\phi_2(r_2)|H_{12}|\phi_1(r_1)\phi_2(r_2)\rangle \\
&+ \langle\phi_2(r_1)\phi_1(r_2)|H_{12}|\phi_2(r_1)\phi_1(r_2)\rangle \\
&\pm \langle\phi_1(r_1)\phi_2(r_2)|H_{12}|\phi_2(r_1)\phi_1(r_2)\rangle \\
&\pm \langle\phi_2(r_1)\phi_1(r_2)|H_{12}|\phi_1(r_1)\phi_2(r_2)\rangle\Big]
\end{aligned} \tag{2.16}
$$

We will gather this result into 4 parts and sum it up as the total energy. The energy of first electron (E_1) and second electron (E_2), Coulomb repulsion between them (K), and purely quantum mechanical result called exchange interaction (J).

$$E_1 = \langle\phi_1(r_1)|H_1|\phi_1(r_1)\rangle = \langle\phi_1(r_2)|H_2|\phi_1(r_2)\rangle \tag{2.17}$$

$$E_2 = \langle\phi_2(r_1)|H_1|\phi_2(r_1)\rangle = \langle\phi_2(r_2)|H_2|\phi_2(r_2)\rangle \tag{2.18}$$

$$
\begin{aligned}
K &= \langle\phi_1(r_1)\phi_2(r_2)|H_{12}|\phi_1(r_1)\phi_2(r_2)\rangle \\
&= \langle\phi_2(r_1)\phi_1(r_2)|H_{12}|\phi_2(r_1)\phi_1(r_2)\rangle
\end{aligned} \tag{2.19}
$$

$$
\begin{aligned}
J &= \langle\phi_1(r_1)\phi_2(r_2)|H_{12}|\phi_2(r_1)\phi_1(r_2)\rangle \\
&= \langle\phi_2(r_1)\phi_1(r_2)|H_{12}|\phi_1(r_1)\phi_2(r_2)\rangle
\end{aligned} \tag{2.20}
$$

$$E = E_1 + E_2 + K \pm J \tag{2.21}$$

We notice the plus and minus sign in exchange interaction (J). This is due to the symmetry/antisymmetry requirement of the boson and fermions we described. So, for the triplet state, the spin part is symmetric, which means the interchange of the electrons will correspond to -J, and for the singlet state, the spatial part is symmetric, which will correspond to +J. In the case of two hydrogen atoms with two electrons the total energy of the system for the triplet state is lower than the singlet state by 2J (for positive J), and the difference between triplet and singlet

states finds the exchange energy J. Since the same spin causes the electrons to spread farther apart due to reducing Coulomb repulsion, positive J favors the triplet state which is in agreement with Hund's first rule. When the electrons on neighboring atoms, however, a state centered on one atom and a state centered on the other will combine to form a joint state. Due to the fact that kinetic energy is increased when the particle is squeezed inside a smaller box, electrons form bonds (molecular orbitals) to increase the size of the box and reduce the kinetic energy. These molecular orbitals can either be bonding (spatially symmetric, spin singlet) or antibonding (spatially antisymmetric, spin triplet). The antibonding orbitals are more energetically costly, because of greater curvature and hence larger kinetic energy, and due to negative exchange integral, the singlet state is favored in the case of hydrogen molecule. Thus the exchange interaction can be defined as:

$$J = \frac{E_S - E_T}{2} \tag{2.22}$$

We can express the same result with integral notation [96]. Energies of the singlet and triplet states are given.

$$E_S = \iint \psi_S^* \hat{H} \psi_S \, \mathrm{d}\mathbf{r}_1 \, \mathrm{d}\mathbf{r}_2, \tag{2.23}$$

$$E_T = \iint \psi_T^* \hat{H} \psi_T \, \mathrm{d}\mathbf{r}_1 \, \mathrm{d}\mathbf{r}_2. \tag{2.24}$$

The energy difference between singlet and triplet states is given.

$$E_S - E_T = 2 \iint \psi_a^*(\mathbf{r}_1) \psi_b^*(\mathbf{r}_2) \hat{H} \psi_a(\mathbf{r}_2) \psi_b(\mathbf{r}_1) \, \mathrm{d}\mathbf{r}_1 \, \mathrm{d}\mathbf{r}_2. \tag{2.25}$$

The equation for the spin part, considering the normalization condition, gives the energy difference between singlet and triplet states.

$$J = \frac{E_S - E_T}{2} = \iint \psi_a^*(\mathbf{r}_1) \psi_b^*(\mathbf{r}_2) \hat{H} \psi_a(\mathbf{r}_2) \psi_b(\mathbf{r}_1) \, \mathrm{d}\mathbf{r}_1 \, \mathrm{d}\mathbf{r}_2. \tag{2.26}$$

Excluding all the constant terms, exchange integral J is defined as:

$$J = \frac{E_S - E_T}{2} = \iint \psi_a^*(\mathbf{r}_1)\psi_b^*(\mathbf{r}_2)\hat{H}\psi_a(\mathbf{r}_2)\psi_b(\mathbf{r}_1)\,\mathrm{d}\mathbf{r}_1\,\mathrm{d}\mathbf{r}_2. \tag{2.27}$$

Although it is relatively simple to derive, a solution for any realistic system is impossible due to complexity of the many-body wavefunction. Instead, we will use a DFT code which is a very successful method for calculating magnetic properties of solids [92]. Also, DFT made no assumptions on whether the atoms are localized or itinerant, DFT checks the final energy of the system using electron density. There are more accurate methods such as the Monte-Carlo method but it is more expensive than DFT, so by means of computational time and accuracy performance we can argue, DFT is one of the best tools.

The exchange integral J in Eq. 2.27 is equivalent to the exchange constant in the model proposed by Heisenberg in 1928 to explain ferromagnetic and antiferromagnetic materials [97].

$$\hat{H} = -J \sum_{\langle i,j \rangle} \mathbf{S}_i \cdot \mathbf{S}_j \tag{2.28}$$

In our DFT calculations, we calculated the total energy difference between antiferromagnetic and ferromagnetic alignments to calculate the exchange energy. We achieved it by giving initial non-zero magnetization on dimers and checking the final magnetization at the end of the calculation, calculating the total energy. The difference between the total energies will correspond to the exchange energy J in the Heisenberg Hamiltonian. If the J is larger than 0 then we have a ferromagnetic system and for the case when it is less than 0, the system is antiferromagnetic. If the energy difference of FM and AFM configurations is zero, then we conclude that J=0 and the system is nonmagnetic.

$$J = E_{xc} = \frac{E_{AFM} - E_{FM}}{2} \tag{2.29}$$

Chapter 3

Results

3.1 Quantum Espresso

There are many different codes for electronic structure calculations employing density functional theory. These codes differ from each other depending on their basis sets (plane-wave basis set, atom-centered basis set, real space grids, etc.), potentials used to represent core electrons (all-electron, pseudopotentials, Gaussian type, etc.), and license (open-source or commercial). We study properties of dimer dopants of 2 transition metal pairs (Fe, Cr, Co, and V) in the near and far configuration using a community-supported density functional theory code, Quantum Espresso (QE) (opEn-Source Package for Research in Electronic Structure, Simulation, and Optimization) [98, 99, 100] version 7.2. QE is a plane wave basis software package used for *ab initio* calculations. A plane-wave basis set has many advantages, such as high efficiency in periodic systems, mainly because of the easier handling of integration and derivation, which are commonly used in density functional theory calculations. QE uses different types of pseudopotentials (such as norm-conserving, projected-augmented (PAW), and ultra-soft (USPP)) to represent the core electrons that are considered to be frozen. We use ultra-soft pseudopotentials for the core electrons and local density approximation (LDA) for the exchange-correlation potential.

3.2 Convergence Tests

Various parameters given in the input file can alter the accuracy of the results. The QE software already defines certain default values for all of these input parameters. However, these default values are only rough estimates and cannot be used for all the systems investigated. The best practice would be conducting convergence tests for the most important input parameters. A convergence test for a parameter is conducted by increasing the parameter until the improvement in the energy is below a certain value. This ensures the calculation is accurate enough, and larger computational resources are not needed for these calculations because after this threshold, the improvement saturates, and increasing the parameter further will only cost more computationally with a minimal benefit. Such threshold is called the cutoff value, and the converged parameter is taken from the subsequent calculations. We used 0.1 meV per unit increase in the input parameter criterion for our convergence tests. Additionally, we use certain default values as input, such as the convergence criterion for the electron kinetic energy is taken as 10^{-6} Ry for self-consistent calculations, a mixing ratio of 0.7 is taken for the mixing of the electron density in each self-consistent cycle with the local-TF mixing mode. Smearing is usually not a crucial parameter for this thesis since the host material, GaAs, is a semiconductor. As a result, we take the default value of Gaussian smearing with 0.01 Ry for self-consistent and band structure calculations. For the total and projected density of states we use the tetrahedron smearing. Furthermore, in relaxation calculations, we use the Broyden–Fletcher–Goldfarb–Shanno (BFGS) algorithm for ion dynamics and structural relaxation, which is a quasi-Newtonian iterative technique. The convergence criteria for energy is 10^{-4} Ry, and for force, 10^{-3} Ry/Bohr. We report the relaxed positions of atoms of the TM dimers on GaAs(110) surface in Chapter 4.

We focus on converging 4 input parameters, which are energy cut-off for wavefunctions (ecutwfc), number of k-points (k-point), lattice parameter, and the vacuum distance. The parameter ecutwfc represents energy values of wavefunctions as QE uses a plane wave basis. Depending on the value of the energy cut-off

the calculation employs more and more plane waves such that the accuracy of results is improved by reducing the total energy. We have found the parameter ecutwfc 100 Ry in Fig. 3.1. So only the plane waves with kinetic energies smaller than the cutoff energy value are included. The cutoff energy E_{cut} is defined as

$$E_{cut} \geq \frac{1}{2}|\mathbf{k} + \mathbf{G}|^2 \tag{3.1}$$

Another input parameter depending on the ecutwfc is the cut-off energy for charge densities (ecutrho). Different values are required for different pseudopotentials. As we employ ultra-soft pseudopotential we use 8 times the converged ecutwfc values, which is 800 Ry.

A third parameter is the number of k-points that is related to the sampling of the reciprocal space. The total electron density is calculated by integrating the magnitude of wavefunctions of all occupied states in the first Brillouin zone. With more k-points and a denser k-point grid, we have a higher accuracy of integration in the Brillouin zone. However, this requires more computational time. Our convergence calculation for the optimum number of k-points yields 6x6x6 in bulk and 2x2x1 in surface with a uniform Monkhorst-Pack grid around the zone center (k=0).

After the energy cutoff and k-point value, the lattice parameter of the system needs to be calculated with it because it will be different for different pseudopotentials and different system settings. Although it does not represent the error margin of the rest of the calculation, the calculated lattice parameter is generally seen as a measure of validity since the lattice parameter of a crystal can be measured experimentally using X-ray diffraction and can be compared with the calculation. In our calculations, we have found the lattice parameter as 5.68742 Å which differs from the experimental value of 5.65325 Å [81] by only with 0.6 % . For calculation of the relaxed lattice parameter we calculate the total energy of the system for different lattice parameter inputs and we use the post-processing tool ev.x (included in the Quantum Espresso software kit), which employs Birch 3rd-order fitting for the equation of state. We demonstrate the ecutwfc and lattice parameter convergence results in Fig. 3.1. In surface calculations, we also employed a 12 Åvacuum distance between subsequent images of the unit cells

along the z-axis to avoid interactions.

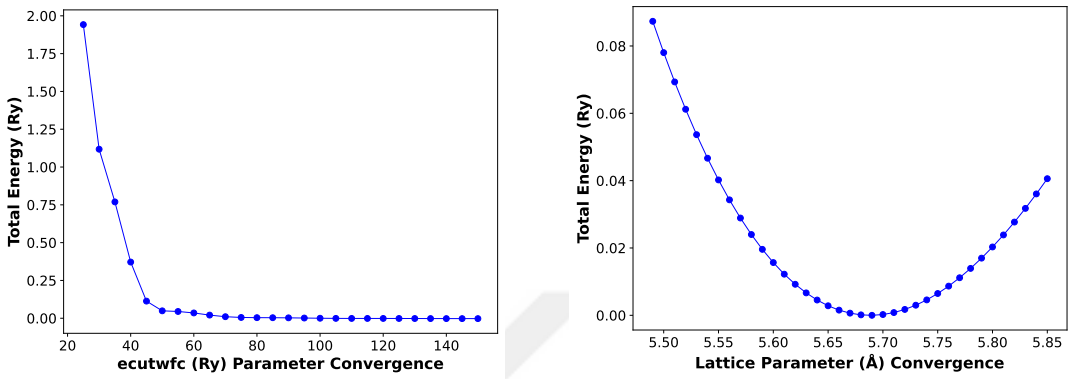

(a) (b)

Figure 3.1: Convergence test results for (a) energy cutoff, and (b) lattice parameter. Since the total energy varies with different pseudopotentials we subtract the minimum values of the graph for simplicity. Substracted values for (a), -762.90953282 Ry and for (b), -5980.26600061 Ry.

3.3 Slab Configuration

We start our calculations by modeling the GaAs surface starting from the bulk system with a software package called BURAI. Modeling the system for a DFT calculation starts with a crystallographic information file (CIF). This CIF file provides the atoms' positions within the unit cell. Using a CIF file with a conventional cell for GaAs, we construct a 2x2x2 supercell by transforming the primitive lattice vectors (Fig. 3.2). Then, we construct the (110) surface with 7 atomic layers from this supercell. Finally, we end up with a slab configuration with 112 atoms . We have not converged the number of layers for the surface, it had been done in the literature and most of the calculations use a typically 6 or 7 layered surface [101]. To simulate surface effects (most significantly relaxed atomic positions) and obtain surface relaxation, simulations are carried out by fixing the bottom 4 layers and freeing up the upper 3 layers. This ensures the simulation of a free surface that is attached to bulk system, mimicking the semi-infinite nature of the system. We also add a 12 Å vacuum region between top and bottom surfaces in order to prevent interaction of two surfaces with each other as shown

in Fig. 3.3. We substitute two adjacent Ga atoms with a transition metal (Fe, Co, Cr, or V) in two different configurations: near and far configuration. There are two different separations for Ga atoms on (110) surface. We name the one in Fig. 3.3 c and d as near configuration and far configuration, respectively, due to small and large distances. Our goal is to study the change in the strength of the exchange interaction as a function of the dimer distance.

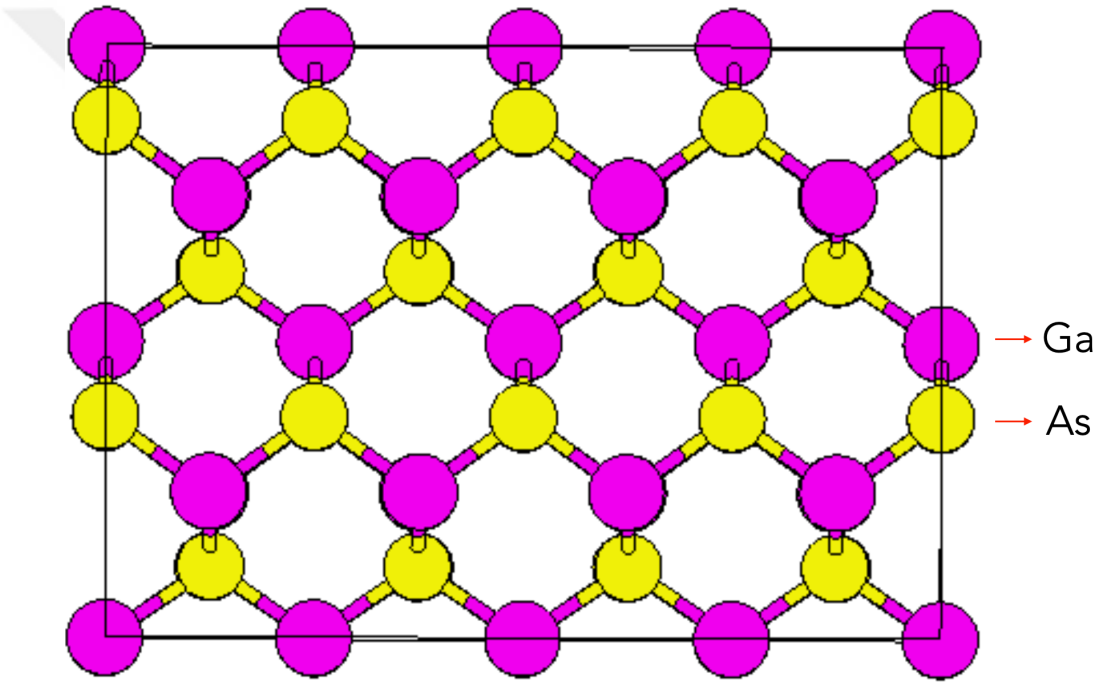

Figure 3.2: Top view of the supercell of GaAs(110) surface. Here yellow atoms represent As and pink atoms are Ga.

After we model the GaAs(110) surface and add substitutional transition metal dopants, we carry out and report several calculations such as structural relaxation, exchange energy between dimer atoms, and magnetic and electronic calculations, including spin-resolved DOS & PDOS projections. Additionally, we also report calculations regarding the topographical images of the surface with TM dopants. Experimentally, one can measure the electron density by scanning tunneling microscopy (STM); obtaining the result by computation is useful so that DFT and STM results can be used to validate each other.

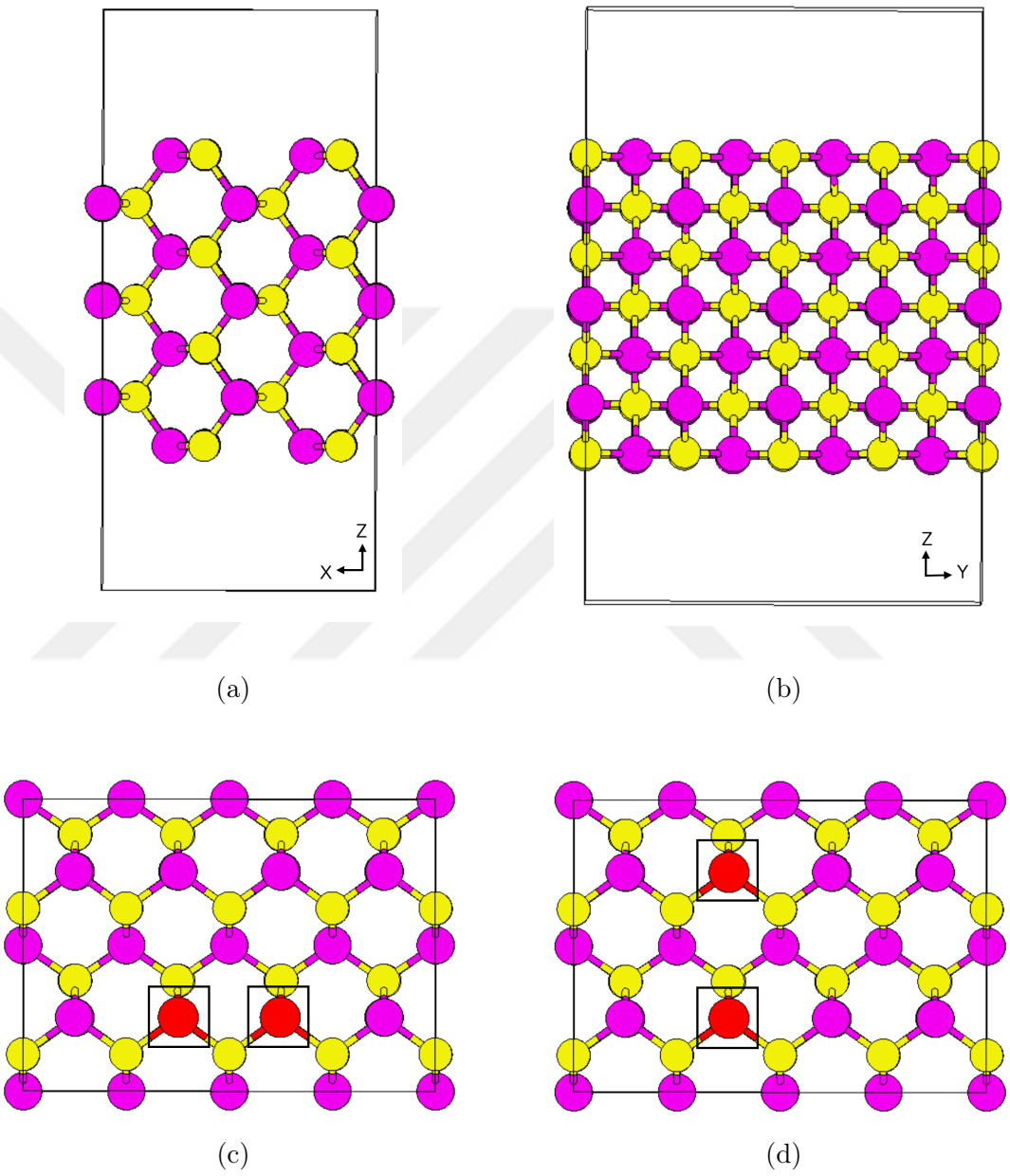

(a) (b)

(c) (d)

Figure 3.3: In (a) and (b) we show the supercell from side views. The supercell size for x, y and z axes are 11.374 Å , 16.086 Å , 24.137 Å respectively. (c) and (d) demonstrate the near and far configuration dimer doping from the top view respectively. The distance between the dimers is 3.977 Å for near configuration and 5.687 Å for far configuration.

3.4 Relaxation Results

First, we report the results of the structural relaxation calculation. We first calculate the relaxation of the pure GaAs surface along (110) direction with 112 atoms. The relaxation shows a buckling angle of 27 degrees, which is in excellent agreement with the previous calculations and experimental measurements [102]. Then, we continue to relax this surface with TM dimers by substituting TM elements with Ga.

We observe different atomic positions after relaxing atoms on ferromagnetic and antiferromagnetic configurations. In ferromagnetic configuration, dopants are farther apart relative to antiferromagnetic alignment. This is also what we expect since the Pauli exclusion principle based on the Coulomb repulsion of the same spin elements is expected to force ferromagnetic (triplet, S=1) configurations to stay away from each other. On the other hand, it favors the formation of antiferromagnetic (singlet, S=0) alignment. A model of the relaxation and definition of related distances can be found in Figure 3.4 focusing around the dimer atoms.

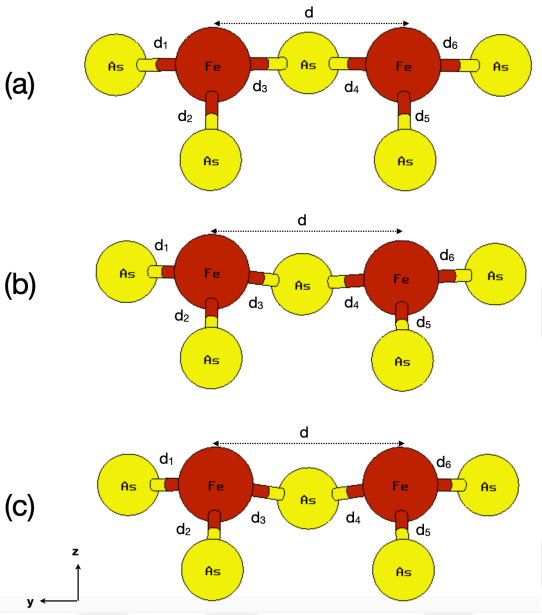

Figure 3.4: Comparison of final atomic positions for ferromagnetic and antiferromagnetic alignments of a typical transition metal dimer, in figure it is Fe dimers on near configuration after the relaxation calculations. (a) initial positions, (b) ferromagnetic relaxed positions, and (c) antiferromagnetic relaxed positions. d represent the distance between dimers; d_1, d_2, d_3 represent the distance between Fe atom and surrounding As atoms, and d_4, d_5, d_6 represent other Fe atom and surrounding As atoms.

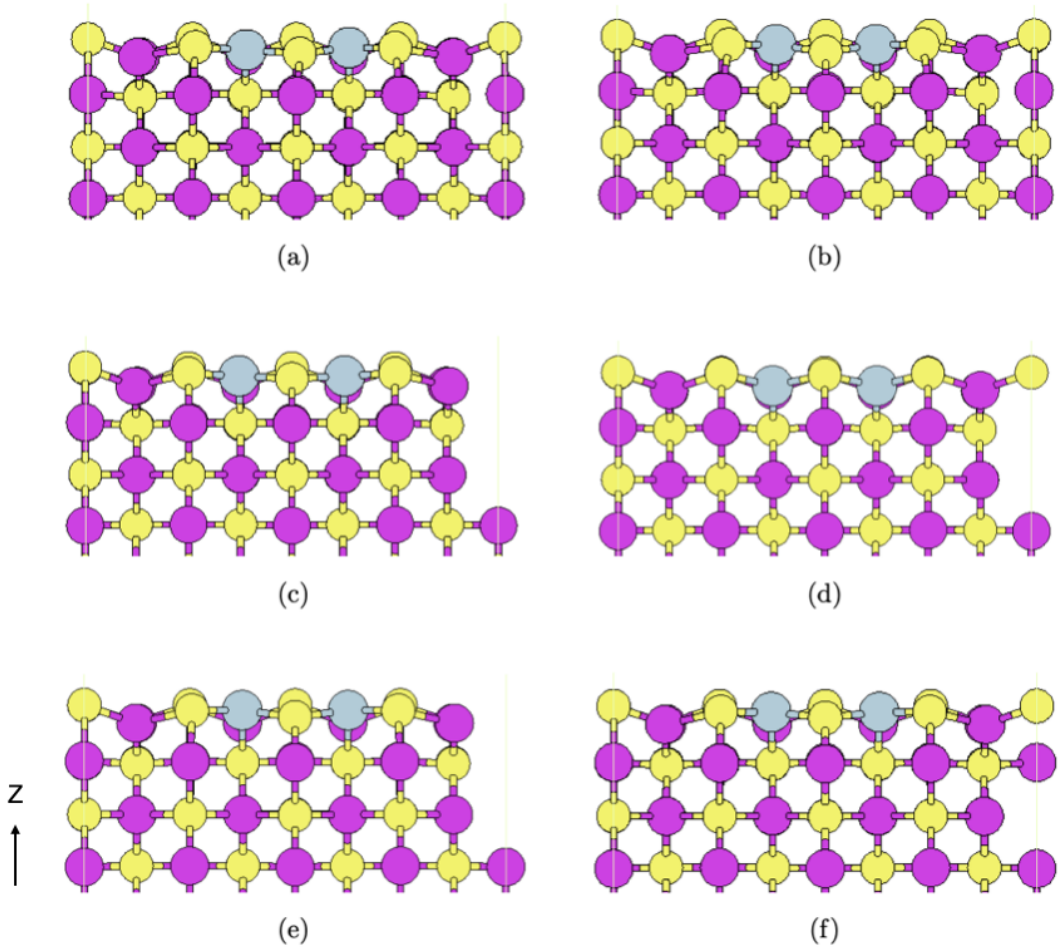

Figure 3.5: Relaxed positions of Fe, Cr, V dimers in ferromagnetic and antiferromagnetic alignments. Pink atoms represent Ga, yellow atoms represent As, and blue atoms are the dimer atoms. (a) Fe ferromagnetic, (b) Fe antiferromagnetic alignments. (c) Cr ferromagnetic, (d) Cr antiferromagnetic alignments. (e), and (f) V ferromagnetic and antiferromagnetic alignments, respectively.

Figure 3.5 demonstrates the topmost 4 layers of the 7-layered slab along the slab direction, corresponding to the z-axis. The bottom 3 layers, which have been kept fixed, are not shown in this figure since they do not relax. We observe that dimer dopants are in a relatively higher position in the z direction compared to Ga atoms generally. The largest height difference is observed on Vanadium (V) dimers. For the relaxations of Cr dimers, relative positions differ notably between ferromagnetic and antiferromagnetic alignments. As shown in Table 3.1,

for Fe dimer in the near configuration (dimer distance = 3.9772 Å), the relative displacement of the FM and AFM configurations are positive and negative, respectively, indicating the two atoms move closer in the case of AFM contrary to FM. Additionally, for the FM alignment, all the distances are different from each other after relaxation, whereas for AFM alignment, we see that some symmetry is preserved. Distances between dimer atoms and As atoms towards bulk are the same (d_2=d_5) Similarly distances between dimer atoms and the nearest As atom on the surface are also same (d_3=d_4). We also observe that relaxed distances between dimer atoms and outermost As atoms are same as well (d_1=d_6).

	Initial (Å)	Relaxed FM (Å)	Relaxed AFM (Å)	Relative Displacement FM (Å)	Relative Displacement AFM (Å)
d	3.9772	3.9962	3.8568	0.019	-0.1204
d_1	2.4899	2.2483	2.1972	0.019	-0.1204
d_2	2.4542	2.2863	2.2369	-0.1679	-0.2173
d_3	2.4542	2.2419	2.1859	-0.2123	-0.2683
d_4	2.4542	2.1694	2.1859	-0.2848	-0.2683
d_5	2.4542	2.2346	2.2369	-0.2196	-0.2173
d_6	2.4899	2.1839	2.1972	-0.306	0.2972

Table 3.1: Relaxed positions of Fe dimer in near configuration. Initial positions are given compared to relaxed ferromagnetic and antiferromagnetic configurations. Also, relative displacement values for Fe dimers for near configuration are reported.

Next, we report the far configuration results with the same methodology. In the case of far configuration (dimer distance = 5.6874 Å) for Fe as shown in Table (3.2) we observe practically no difference between FM and AFM relaxations. We still observe the buckling of the surface atoms which changes all the distance except for the dimer distance, however, dimer distance (d) changes insignificantly. This clearly indicates that the magnetic interaction between magnetic dopants which depends on their distances plays a significant role on their relaxed positions in a

crystal. In the far configurations we see a more symmetric relaxation compared to the near results in Table 3.1. Especially relaxed FM positions are similar to each other compared to relaxed AFM position on the contrary to near relaxed positions. We will talk about the exchange interaction in the case of far and near configurations in following sections of this thesis.

	Initial (Å)	Relaxed FM (Å)	Relaxed AFM (Å)	Relative Displacement FM (Å)	Relative Displacement AFM (Å)
d	5.6874	5.6873	5.6874	-0.0001	0
d_1	2.4899	2.2745	2.2759	-0.2154	-0.214
d_2	2.4542	2.2745	2.2760	-0.1797	-0.1782
d_3	2.4542	2.2976	2.3010	-0.1566	-0.1532
d_4	2.4899	2.2745	2.2759	-0.2154	-0.214
d_5	2.4542	2.2745	2.2760	-0.1797	-0.1782
d_6	2.4545	2.2976	2.3009	-0.1566	-0.1533

Table 3.2: Relaxed positions of Fe dimer in far configuration. Initial positions are given with comparison to relaxed ferromagnetic and antiferromagnetic alignments. Also, relative displacement values for Fe dimers for far configuration are reported.

We also report relaxation results for the Cr dimer, Co dimer, and V dimer pair positions in Table A.1, Table A.2, and Table A.3 in the Appendix, respectively. These results resemble Fe dimer outcomes such that antiferromagnetic alignments are closer to each other compared to ferromagnetic alignments. Similarly, relaxed positions of far configurations are very close to each other for both alignments regardless of the spin singlet or triplet configurations as seen for the Fe dimer. In all these calculations we start with the same initial values for dimer distances as shown in Table 3.2 and Table 3.1 It looks like initial distances are increased for Cr and V pairs, whereas it decreased for Co pair which has zero magnetic moment as we show in the next section below.

3.5 Magnetic moment results

For each dimer configuration, we start with a guess for the magnetization of each atom. We set the magnetization for Ga and As atoms as zero and take an approximate value for the TM atoms based on the number of unpaired electrons. That's called starting magnetization. For ferromagnetic configurations, we set the same sign and magnitude for two TM atoms, whereas we set the signs opposite for the antiferromagnetic configurations. QE runs collinear spin-polarized calculations (also known as LSDA), which do not contain relativistic effects.

	FM-Near	AFM-Near	FM-Far	AFM-Far
Fe_1	1.29	2.00	2.49	2.52
Fe_2	2.02	-2.00	2.49	-2.52
Cr_1	-2.80	-2.90	-2.87	-2.88
Cr_2	-2.80	2.89	-2.87	2.88
V_1	1.69	1.70	1.67	1.68
V_2	1.69	-1.70	1.67	-1.68
Co_1	0.00	0.03	0.00	-0.00
Co_2	-0.00	-0.03	0.00	0.00

Table 3.3: Magnetic moments of TM Dimers, Fe, Cr, V, and Co (in μ_B)

From the Table 3.3 we first notice that, Co magnetic moments are practically 0 for all configurations. This is in agreement with our exchange energy results since there is no magnetic moment difference of the ground state energy. Because of this reason we do not report electronic or exchange results for Co in the rest of this thesis. For all of AFM alignments we notice among the dimers the magnetic moments equal in magnitude and opposite in sign which is in excellent agreement with AFM configuration property of a system. However, in the case of ferromagnetic alignment in the near configuration two Fe atoms have different magnetic moments. We have tried with many other relaxation methods and got a similar result in all of them. On the other hand, except the Fe dimer, on near and far

configurations dimers have similar magnetic moments. We also observe that for Fe dimers, the relaxed final magnetic moments of Fe dopants in the far configurations are generally larger than the near configuration for both ferromagnetic and antiferromagnetic alignments.

3.6 DOS & PDOS Projections

In this section we report the total density of states (DOS) and projected density of states (PDOS) of 16 different configurations. First, we report the pure GaAs DOS. Afterward, two configurations; near and far, and two alignments; ferromagnetic and antiferromagnetic DOS and PDOS are reported. PDOS calculations are essential to explain the origin of the exchange splitting. The first thing we notice from doped systems is that antisymmetric behavior starts to emerge around the Fermi level. The second important observation is that s and p orbitals of the TM dopants do not contribute to the total DOS of the system. They are either too deep in the valence band or too far at the conduction band with insignificant amplitudes. We do not include any of these projections in this thesis, however, as an example, one can see the magnitude of these orbitals in the Appendix section, Figure B.1 for the case of iron dimers. The results for other TM dimers are very similar in behavior to the Fe dimers. Additionally, the magnitude of the exchange energy (as seen in Table 3.4) is negligible for the Co dimers, as well as the magnitude of the magnetic moments. This dimer pair does not exhibit strong magnetic behavior. Thus, it is not included in the rest of the thesis. Instead, we compare pure GaAs DOS with Fe, Cr, and V dimers. Throughout this section, we report DOS/PDOS of the near configuration of TM dimers since far configurations exhibit almost exactly the same behavior. This is quite expected as the electronic structure in DFT depends on the electron density which changes only by a fraction as two atoms are separated by a small distance in a 112 atom supercell. Lastly, in all figures that are reported in this section, we use a moving average method with a window size of 10 for all of the projections.

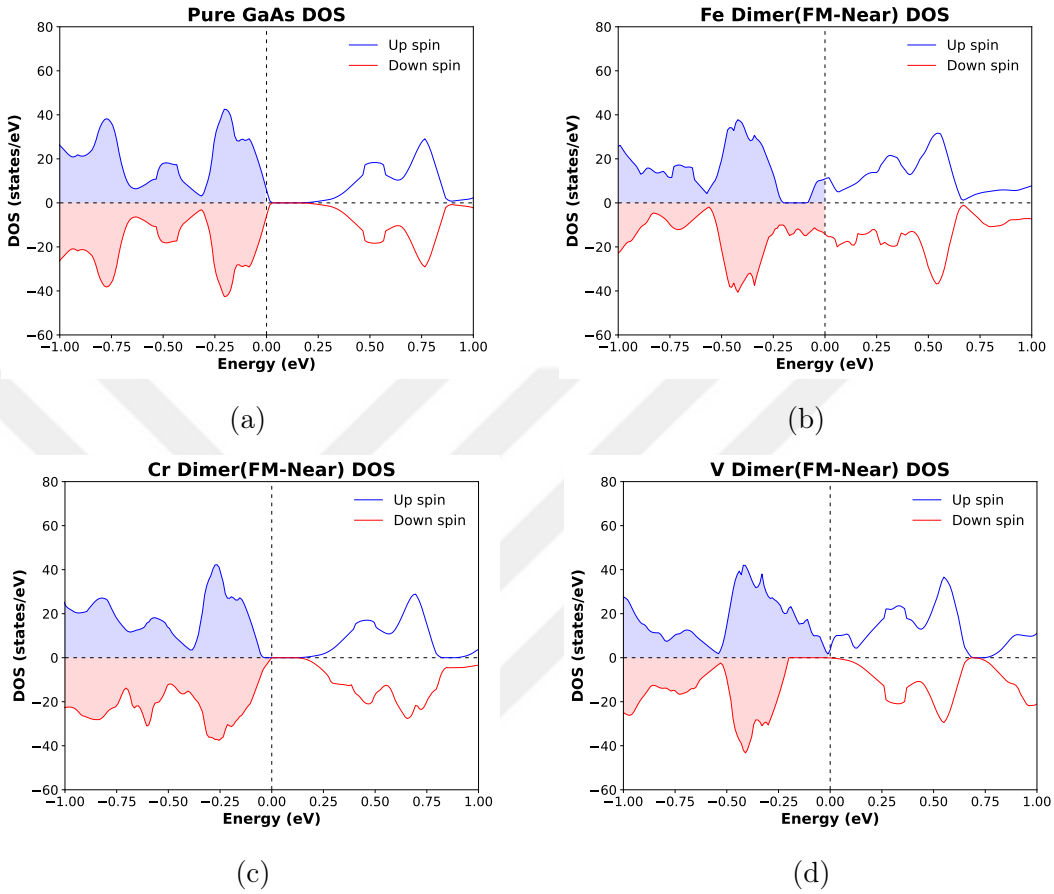

Figure 3.6: DOS results for 112 atoms GaAs(110) surface. (a) pure GaAs configuration. (b) Fe dimer ferroamagnetic near configuration. (c), and (d) Cr and V dimer ferromagnetic near configurations respectively. Figures demonstrate the in-gap states and magnetic behavior around the Fermi level (dashed line).

In general, one can say that states that appear in the band gap region of dimer-doped GaAs originate from the d orbitals of the TM dimers that they belong to. In Figure 3.6 (a), we note two important projection characteristics for pure GaAs. The first one is the band gap being smaller than the experimental band gap which is a well-known underestimation problem of the DFT calculations. The second is the symmetrical behavior of the up and down spin densities. By looking at this projection, we can conclude that it is a non-magnetic semiconductor since the total spins and magnetic moments in this material cancel out. Once we introduce two TM atoms as substitutions to the Ga atoms, we observe a dramatic change

in the DOS especially around the Fermi level. As shown in Figure 3.6 (b) the addition of Fe dimers does not only cause GaAs to be a magnetic material but also turns it a metallic system. The Fermi level crosses the energy levels of states that originate from the Fe dimers. In the case of Cr dimers shown in Figure 3.6 (c), we observe a semiconducting phase with a slightly smaller band gap. On the other hand, doping with V dimer turns GaAs a half-metal, namely a metallic system which only has one type of spin at the Fermi level as shown in Figure 3.6 (d). Half-metallic systems are perfect materials for spin filters and sources of pure spin currents. Such significant changes in the electronic structure with less than 1.79 % % of dopants is an outstanding result that we report here. As shown in Figure B.1 in Appendix section, s and p orbitals of TM dopants do not contribute significantly to the DOS of the TM doped GaAs, thus, all of the new features should come from the d orbitals of the dimers, which we discuss below.

Next, we examine orbital projections (d-PDOS) of states around the Fermi level to show their origins for near ferromagnetic configuration. We again position the pure GaAs in Figure 3.7 (a) and look more closely at the differences around the Fermi level for dimers. Figure 3.7 (b) shows Fe dimer and around Fermi level we observe two distinct down spin peaks before and after Fermi level. Around Fermi level we can say the system is down spin polarized and amplitudes are showing us that in-gap states, states that make the system metallic as we see from figure 3.6 (b) is due to d orbitals of Fe dimers. In 3.7 (c) we are looking at Cr dimers. We noticed two important things in this plot. First, the system gains half-metallic behavior just before the Fermi level with down spin polarization, and a bandgap following another down spin half-metallic behavior. This means this system has both a semiconductor and a half-metallic properties. These means we can manipulate this semiconductor with applying bias voltages to obtain single type spin states. In Figure 3.7 (d) we look at V dimers d-PDOS. This system has a up spin half-metallic character around Fermi level with a distinct up spin peak just before Fermi level. This figure clearly shows that new features that are added to the pure GaAs with TM dimers originates from the d orbitals of the dopants.

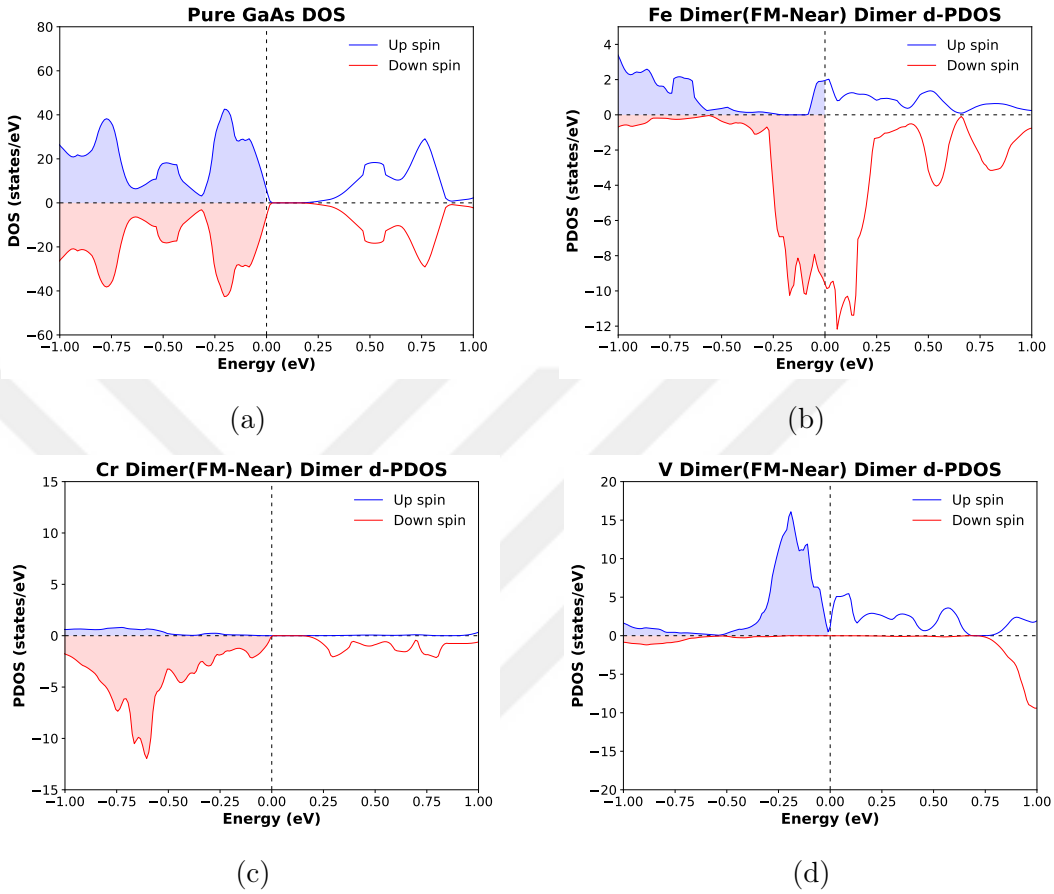

Figure 3.7: Pure GaAs(110) and dimers' d-PDOS projections for near ferromagnetic configuration. (a) Pure GaAs(110). (b) Fe dimer' d-PDOS. (c) for Cr and (d) for V dimer d-PDOS on ferromagnetic near configuration. Fermi level (dashed line).

Next, we present the d-PDOS projections for Fe dimers on near configuration in Figure 3.8. (a) shows dopant 1 d-PDOS on ferromagnetic alignment. We observe two distinct peaks just before and after the Fermi level with down spin polarization. (b) demonstrates same alignment but for dopant 2. We observe similar behavior in this projections, down spins are dominant with similar amplitute and similar occurrences. For both of the projections, we see similar up spin distribution. Dopant 2 has slightly higher down spin polarization than dopant 1 which means dopant 2 has higher magnetic moment which is in agreement with the magnetic moment table we provided 3.3. From Figure 3.8, we demonstrate

d-PDOS projections of Fe dimers on (a) for dopant 1 and (b) for dopant 2 in antiferromagnetic alignment. We observe, down spin polarization for dopant 1 in (a), and up spin polarization for dopant 2 in (b). This is in agreement with the antiferromagnetic setting since we are expecting non-zero magnetism in pairs but with opposite signs. This plot also shows localized characteristics near the Fermi level which is in agreement with localized characteristics of d orbitals. These states can be used in electron trapping.

Next, we provide detailed projections in the appendix, which we will briefly mention here. In Figure B.3 we investigate antiferromagnetic alignments DOS of dimers. (a) shows pure GaAs for comparison. (b) shows Fe dimer which metallic behavior is almost exactly same as ferromagnetic alignment. It differs with symmetric behavior of spin polarization due to antiferromagnetic nature. In (c) we show Cr dimer. We see bandgap significantly reduced compared to ferromagnetic alignment and we noticed the fully symmetric spin polarization. In (d) we see V dimer in antiferromagnetic alignment. Half-metallic behavior vanishes in this projection and a non-magnetic semiconductor with almost negligible band gap noticed. Next figure from appendix is Figure B.3 shows antiferromagnetic alignment d-PDOS results for dimers with (a) pure DOS comparison. In (b) we show Fe dimer d-PDOS which is non-magnetic metallic with a sharp peak just around the Fermi level. (c) shows Cr dimer which has almost zero band gap and again non-magnetic and a small peak just after Fermi level. (d) shows V dimer d-PDOS on antiferromagnetic alignment with a distinct peak just before Fermi level following a tiny band gap and fully symmetric spin polarization overall. Next, we look at how subshells distribution among d-PDOS to address any dominant orbital exist and if e and t_2 projections separate from each other. On e and t_2 projections Figure B.5, we observe the down spin polarization near the Fermi level for both of the projections with a double down peak before and after the fermi for e projection in (a). Other than a few up peaks after Fermi level on t_2 projection, (b), the two projections did not separate. On spin polarization, we observe similar trends on dopant 2 e and t_2 projections. We interpret this result as two projections that contribute nearly equally. Similar trends seen on similar projections, in antiferromagnetic alignments B.6. Two projections for the same

dopant contribute the same spin channel. In Figure B.7 we see other dopant contribute equally with opposite sign and the overall system gain non-magnetic characteristics. We also look at more in detail for e and t_2 projections' subshells to see any dominant orbital exist. From Figure B.4 we demonstrate (a) e and (b) t_2 projections. We notice almost no single peak such that all the orbitals contribute total d-PDOS almost equally.

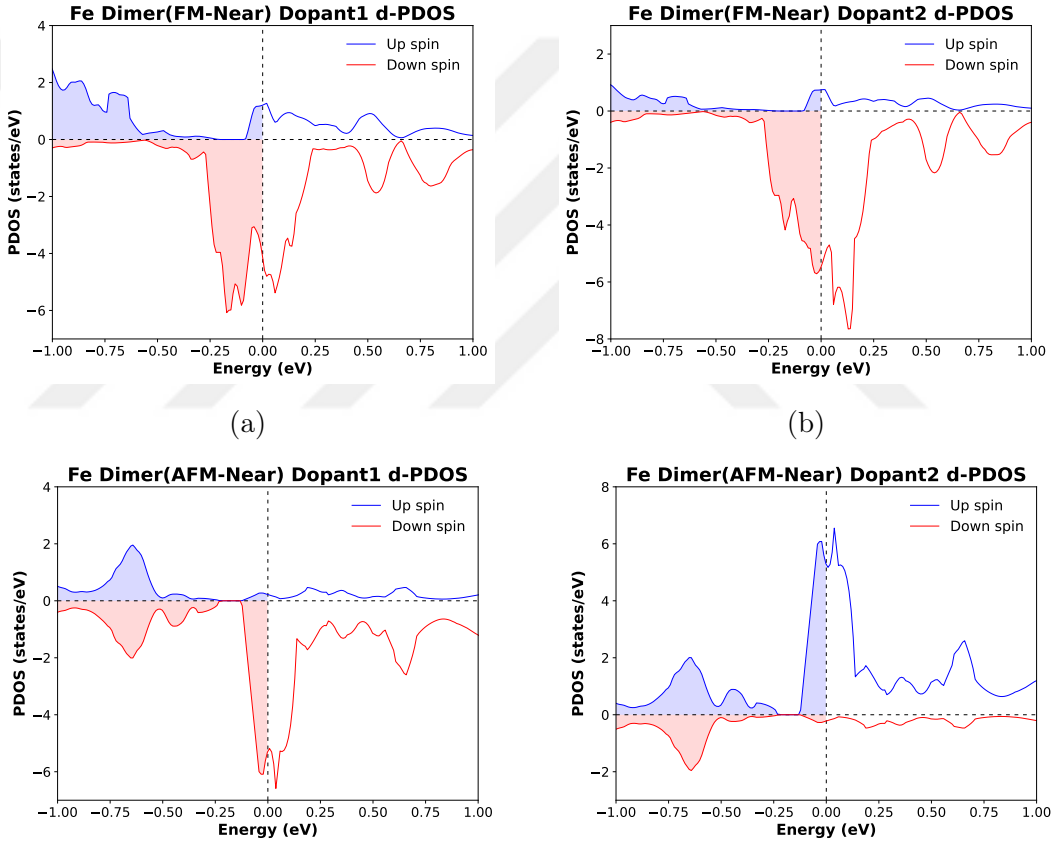

Figure 3.8: d-PDOS projections for Fe dimers on near configuration. (a) and (b) represents ferromagnetic alignment dopant 1 and dopant 2 respectively. (c) and (d) represents antiferromagnetic alignment for dopant 1 and dopant 2 respectively.

3.7 Exchange Energy Calculations

After we reduce the stress inside the unit cell with relaxation calculation, we now report computed exchange energy values by looking at the differences between the final energies of two alignments as shown below:

$$E_{xc} = \frac{E_{AFM} - E_{FM}}{2}. \tag{3.2}$$

The energy difference between singlet and triplet states indicates the ground state configuration of dimers. A negative exchange energy tells us that an antiferromagnetic alignment is preferred and a positive exchange energy indicates that ferromagnetic alignment is favorable. We present 4 different TM dimers (Fe, Cr, Co, V) on near and far configurations with the exchange energy and ground state alignments in Table 3.4.

Dimer Type	Exchange Energy (meV)	Ground State Alignment
Fe	-124.36	Antiferromagnetic
Cr	157.80	Ferromagnetic
Co	-0.06	Antiferromagnetic
V	60.92	Ferromagnetic

Table 3.4: Exchange energy results for Fe, Cr, Co, and V dimers with ground state alignment for near configuration

By looking at the numerical values reported above, we observe the highest exchange energy result obtained for the Cr dimer followed by a relatively close exchange energy value by the Fe dimer with ferromagnetic and antiferromagnetic ground states respectively. V dimer has approximately half of the Fe dimer exchange energy with antiferromagnetic ground state. For Co dimer, the ground state is antiferromagnetic but the exchange energy is insignificant. Next, we report exchange results for far configurations of TM dimers in Table 3.5 to see the dependence of the exchange interaction to the separation between dimers.

Dimer Type	Exchange Energy (meV)	Ground State Alignment
Fe	-1.64 meV	Antiferromagnetic
Cr	-0.94 meV	Antiferromagnetic
Co	-0.03 meV	Antiferromagnetic
V	3.16 meV	Ferromagnetic

Table 3.5: Exchange energy results for Fe, Cr, Co, and V dimers with ground state alignment for far configuration

In far configuration, we notice a dramatic change in exchange energy values. The most striking one with more than 2 orders of magnitude for Cr dimer from 157.80 meV in near configuration to -0.94 meV in far configuration. We notice that for Cr dimer only, with increased dimer separation ground state alignment is changed from ferromagnetic to antiferromagnetic. Fe keep the ground state antiferromagnetic alignment same but exchange energy reduced from -124.36 meV to -1.64 meV on far configuration. V has the highest exchange energy on far configuration with ferromagnetic ground state and 3.16 meV exchange energy which was 60.92 meV on near configuration. For Co, ground state is the same and change in the exchange energy is insignificant.

We notice relative displacement differences between ferromagnetic and antiferromagnetic alignment for near (3.977 Å) and far (5.687 Å) alignments became insignificant. This is due to the exchange energy dependence to the atomic separation. Next section below, we interpolate exchange energy and average distance values between ferromagnetic and antiferromagnetic alignments and come up with the distance dependence of exchange energy. By looking at the average distance between dimers on near and far configurations for ferromagnetic and antiferromagnetic alignments and exchange energy, we simply demonstrate that exchange energy decreases with distance. Exchange energy and average distance results for Fe dimers on near configuration are reported below.

	Near	Far
E_{xc}	-124.36 meV	-1.64 meV
$\bar{d}$	3.9265 Å	5.68735 Å

Table 3.6: E_{xc} and average distance ($\bar{d}$) values for Fe dimer on near and far configurations.

We will calculate the relative exchange energy and relative average distance and the ratio of two will give the relation.

$$\begin{aligned} \Delta E_{xc}(\text{Far} - \text{Near})/\Delta\bar{d}(\text{Far} - \text{Near}) &= 122.72/1.76085 \\ &= 69.693\,\text{meV/Å} \end{aligned} \tag{3.3}$$

An inverse correlation indicates a decrease in the exchange energy with increasing distance. Here we assume a linear dependence of the exchange interaction with respect to TM distance. These results clearly shows that farther separation of dimer pairs results in a very large decrease in the exchange energy even for one Angstrom distance between them.

3.8 STM Calculations

Scanning tunneling microscopy, STM is a key instrument for investigating the electronic structure of surfaces and materials at the nanoscale. STM was invented and implemented in 1982 [103, 104]. Later, two scientist, Gerd Binnig and Heinrich Rohrer from IBM Research Division shared 1986 Nobel Prize in physics for the invention of STM. STM may create nanoscale structures that have never been seen in nature by changing the materials it examines. The STM uses an atomically sharp probe tip, usually made of W or Pt-Ir alloy, attached to a piezo drive [105]. Tip is placed in atomically close contact with the sample and by applying a voltage through the x and y planes it measures the tunneling current along the z-axis produced by overlapping wave functions of tip and sample, and the resultant data mapped to the computer to obtain a topographic image of

the surface of a material. The most popular convention regarding the bias voltage's polarity is that the tip is essentially grounded. The bias voltage V is the sample voltage and if $V > 0$ electrons tunnel through the tip's occupied states to the sample's empty states. For $V < 0$, electrons are tunneling from the occupied states of the sample into the empty states of the tip. This either negative or positive bias will result in two distinct appearances of the atoms, with a positive or negative charge, as can be seen in the figure 3.9 produced by post-processing tools, critic2, and Quantum Espresso tool, pp.x which employs Tersoff-Hamann approximation [106]. In this approximation tunneling current is proportional to the applied bias voltage and to the local density of states around the Fermi level.

$$\rho_{\mathrm{loc}}(r, V) = \sum_{k,n}^{E_F - eV \to E_F} |\psi_{k,n}(r)|^2 \tag{3.4}$$

where only one-electron states with energies between E_F - eV (for applying 1 V bias voltage) and E_F are included by the sum and electron density contributions from all states within 1 eV of the Fermi level are included in local density of states.

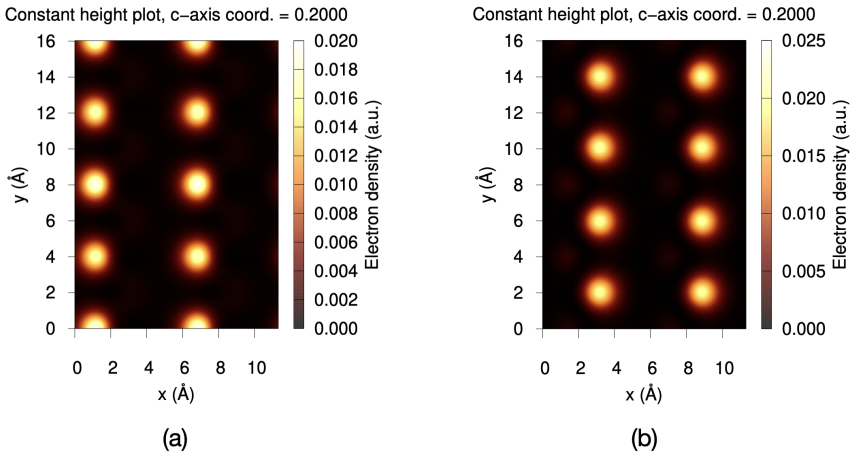

Figure 3.9: STM images, created by post-processing tools pp.x and critic2. Comparison of (a), negative and (b), positive bias of 1 eV on constant height mode.

STM has two modes: constant height and constant current. In constant height mode, the initial height is given, and the probe scans the xy plane with a constant

distance from the sample, projecting the tunneling current along the z-axis. In constant current mode, the tip elongates or contracts in the z-axis to obtain a current through scanning the xy plane, and z values correspond to the distance to obtain the given current.

In STM figures we look at the slab surface from the z-axis. On the other hand x-axis represents x-axis of the unit cell with 11.374 Å and the y-axis represents y-axis in the unit cell with, 16.086 Å. righter color means atoms are closer to surface. Colors in the right-hand on the axis represent the distance to the surface, brighter colors mean, atoms are closer to the surface. We use the trial-error method to find appropriate density in the figures because each plot produces different results for a given density. We pick the densities that produce the best-looking figures. As shown in Figure 3.10 with 1 eV negative bias voltage, we observe the dimers as they are closer to the surface than other atoms as we expect from the relaxed positions in Figure 3.5. In the case of Fe dimers, resolution of the AFM pairs is better in Figure 3.10 (b) compare to FM in part (a). Given the fact that the ground state of Fe dimer is antiferromagnetic (Tables 3.1 and 3.2) this result is what we expect. For Cr and V dimers in Figure 3.10 (c)-(e) we also see dimers easily from our STM calculations. This also opens opportunity to determine location of the TM dimers and even to manipulate their spin states from FM to AFM or vice versa using a spin-polarized STM tip with a small bias voltage.

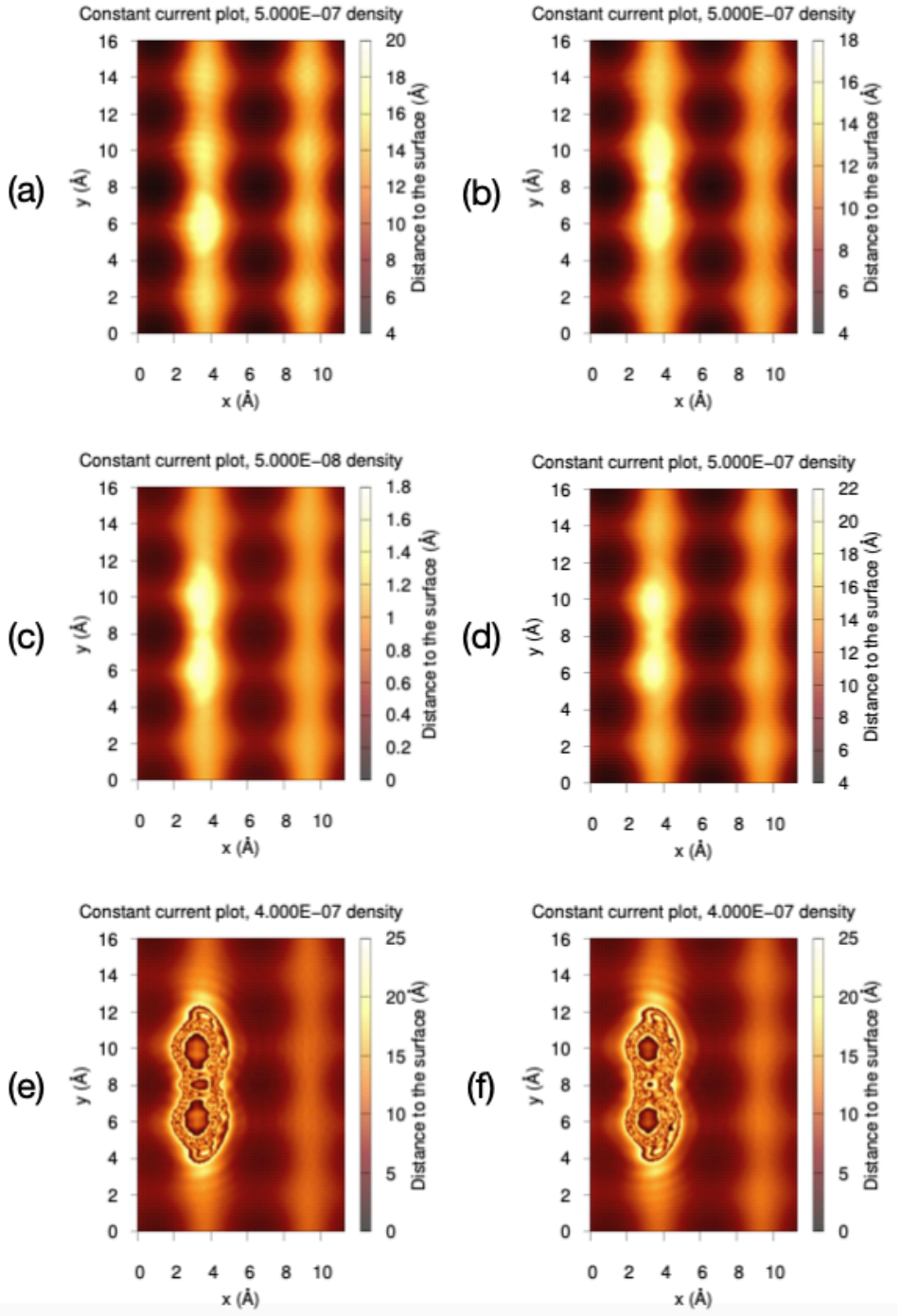

Figure 3.10: STM images created by post-processing tools pp.x and critic2 for 1 eV negative bias and constant current mode. (a) Fe ferromagnetic and (b) Fe antiferromagnetic alignments. (c) Cr ferromagnetic, (d) Cr antiferromagnetic alignments. (e), and (f), V dimers ferromagnetic and antiferromagnetic alignments respectively.

Chapter 4

Conclusion

In this thesis, we investigate dimers on the GaAs (110) surface because of the recent interest in solotronics. In a broad sense, we work in DMS, and the most notable DMS is Mn-doped GaAs, which has been extensively studied in bulk. In the thesis, we differentiate first by studying the (110) surface, then by adding other TM elements (Fe, Cr, Co, V), and finally, by investigating dimers (a pair of dopants) instead of single impurities. We start our calculation by modeling the system with BURAI software package from the conventional unit cell and we build a 2x2x2 supercell. Later, we cut along to (110) surface to have the atomic positions input which has 112 atoms. We use a community-supported DFT software package, Quantum Espresso for simulating systems of our interest. QE uses a plane wave method and we employ LDA exchage-correlation functional and USPP pseudopotential for LSDA calculations. The main subject of this thesis is the exchange interaction between dimers and the relationship between the exchange energy and distance between dimers. We notice reasonable exchange energy on near configurations from highest to lowest, Cr, Fe, V, and insignificant exchange energy and magnetic moment for Co. Also, by comparing exchange energy results on far and near configurations, we demonstrate the exchange energy dependence on distance and show the inverse relation between the two of them. At the end of our exchange energy calculations, we propose that this exchange energies are suitable for use as fast-switching qubits in quantum computing. Also,

these exchange energy values can be checked experimentally using STM. As expected, our DOS calculations show that GaAs is a non-magnetic semiconductor with approximately 0.5 eV band gap. The underestimation of band gap is very much common in LDA, however it can be improved by Hybrid functional which are computationally very expensive. The doping ratio is approximately 1.79 % for dimers and with this ratio, we are able to observe three different characteristics on dimers which are metallic for Fe, semiconductor for Cr, and half-metallic for V. At the end of our calculations, we also generate STM images using post-processing tools with a negative bias voltage of 1 V. Constant current plots show dimers are closer to surface which is in agreement with the relaxed positions that we calculated.

One of the future directions that can be taken is adding on-site correlation effects that are not reflected with LDA by employing the Hubbard+U formalism. Here, we study a single type of atom on dimers, but as we mentioned, co-doping can also yield very interesting results. Other than GaAs, different semiconductors such as ZnS, ZnS, or CdTe can also be studied as host materials, and surfaces can be changed from (110) to (001) (100) or any other relevant experimental direction. Also, we studied four TM, but the rest of the transition metals with non-zero magnetic moments in the periodic table are also open to investigation in the future.

Bibliography

[1] S. Ishii, S. Saiki, S. Onoda, Y. Masuyama, H. Abe, and T. Ohshima, "Ensemble negatively-charged nitrogen-vacancy centers in type-ib diamond created by high fluence electron beam irradiation," *Quantum Beam Science 2022, Vol. 6, Page 2*, vol. 6, p. 2, 12 2021.

[2] V. A. Ivanov, P. M. Krstajic, F. M. Peeters, V. Fleurov, and K. Kikoin, "On the nature of ferromagnetism in dilute magnetic semiconductors: Gaas:mn and gap:mn," *Journal of Magnetism and Magnetic Materials*, vol. 258-259, pp. 237–240, 3 2003.

[3] H. Ohno, "Making nonmagnetic semiconductors ferromagnetic," *Science*, vol. 281, pp. 951–956, 8 1998.

[4] S. Strauf, P. Michler, M. Klude, D. Hommel, G. Bacher, and A. Forchel, "Quantum optical studies on individual acceptor bound excitons in a semiconductor," *Physical Review Letters*, vol. 89, pp. 177403/1–177403/4, 10 2002.

[5] A. Beveratos, S. Kühn, R. Brouri, T. Gacoin, J. P. Poizat, and P. Grangier, "Room temperature stable single-photon source," *The European Physical Journal D - Atomic, Molecular, Optical and Plasma Physics 2002 18:2*, vol. 18, pp. 191–196, 2002.

[6] P. M. Koenraad and M. E. Flatté, "Single dopants in semiconductors," *Nature Materials 2011 10:2*, vol. 10, pp. 91–100, 1 2011.

[7] S. R. Schofield, N. J. Curson, M. Y. Simmons, F. J. Rueß, T. Hallam, L. Oberbeck, and R. G. Clark, "Atomically precise placement of single dopants in si," *Physical Review Letters*, vol. 91, p. 136104, 9 2003.

[8] M. Fuechsle, J. A. Miwa, S. Mahapatra, H. Ryu, S. Lee, O. Warschkow, L. C. Hollenberg, G. Klimeck, and M. Y. Simmons, "A single-atom transistor," *Nature Nanotechnology 2012 7:4*, vol. 7, pp. 242–246, 2 2012.

[9] S. R. Schofield, P. Studer, C. F. Hirjibehedin, N. J. Curson, G. Aeppli, and D. R. Bowler, "Quantum engineering at the silicon surface using dangling bonds," *Nature Communications 2013 4:1*, vol. 4, pp. 1–7, 4 2013.

[10] D. Lee and J. A. Gupta, "Perspectives on deterministic control of quantum point defects by scanned probes," *Nanophotonics*, vol. 8, pp. 2033–2040, 11 2019.

[11] R. Achal, M. Rashidi, J. Croshaw, D. Churchill, M. Taucer, T. Huff, M. Cloutier, J. Pitters, and R. A. Wolkow, "Lithography for robust and editable atomic-scale silicon devices and memories," *Nature Communications 2018 9:1*, vol. 9, pp. 1–8, 7 2018.

[12] C. Bradac, W. Gao, J. Forneris, M. E. Trusheim, and I. Aharonovich, "Quantum nanophotonics with group iv defects in diamond," *Nature Communications 2019 10:1*, vol. 10, pp. 1–13, 12 2019.

[13] T. J. Stock, O. Warschkow, P. C. Constantinou, J. Li, S. Fearn, E. Crane, E. V. Hofmann, A. Kölker, D. R. Mckenzie, S. R. Schofield, and N. J. Curson, "Atomic-scale patterning of arsenic in silicon by scanning tunneling microscopy," *ACS Nano*, vol. 14, pp. 3316–3327, 3 2020.

[14] F. Capasso and A. Y. Cho, "Bandgap engineering of semiconductor heterostructures by molecular beam epitaxy: physics and applications," *Surface Science*, vol. 299-300, pp. 878–891, 1 1994.

[15] F. Tilley, *Theory of Isolated Dopants in GaAs (110) Surfaces*. PhD thesis, University of Leicester, Leicester, UK, September 2015. Department of Physics and Astronomy.

[16] K. Teichmann, M. Wenderoth, S. Loth, R. G. Ulbrich, J. K. Garleff, A. P. Wijnheijmer, and P. M. Koenraad, "Controlled charge switching on a single donor with a scanning tunneling microscope," *Physical Review Letters*, vol. 101, p. 076103, 8 2008.

[17] A. P. Wijnheijmer, J. K. Garleff, K. Teichmann, M. Wenderoth, S. Loth, R. G. Ulbrich, P. A. Maksym, M. Roy, and P. M. Koenraad, "Enhanced donor binding energy close to a semiconductor surface," *Physical Review Letters*, vol. 102, p. 166101, 4 2009.

[18] O. Krebs, E. Benjamin, and A. Lemaître, "Magnetic anisotropy of singly mn-doped inas/gaas quantum dots," *Physical Review B - Condensed Matter and Materials Physics*, vol. 80, p. 165315, 10 2009.

[19] A. M. Yakunin, A. Y. Silov, P. M. Koenraad, J. M. Tang, M. E. Flatté, J. L. Primus, W. V. Roy, J. D. Boeck, A. M. Monakhov, K. S. Romanov, I. E. Panaiotti, and N. S. Averkiev, "Warping a single mn acceptor wavefunction by straining the gaas host," *Nature Materials 2007 6:7*, vol. 6, pp. 512–515, 6 2007.

[20] T. O. Strandberg, C. M. Canali, and A. H. MacDonald, "Magnetic properties of substitutional mn in (110) gaas surface and subsurface layers," *Physical Review B - Condensed Matter and Materials Physics*, vol. 80, p. 024425, 8 2009.

[21] C. Çelebi, J. K. Garleff, A. Y. Silov, A. M. Yakunin, P. M. Koenraad, W. V. Roy, J. M. Tang, and M. E. Flatté, "Surface induced asymmetry of acceptor wave functions," *Physical Review Letters*, vol. 104, p. 086404, 2 2010.

[22] J. M. Jancu, J. C. Girard, M. O. Nestoklon, A. Lemaître, F. Glas, Z. Z. Wang, and P. Voisin, "Stm images of subsurface mn atoms in gaas: Evidence of hybridization of surface and impurity states," *Physical Review Letters*, vol. 101, p. 196801, 11 2008.

[23] G. Balasubramanian, P. Neumann, D. Twitchen, M. Markham, R. Kolesov, N. Mizuochi, J. Isoya, J. Achard, J. Beck, J. Tissler, V. Jacques, P. R. Hemmer, F. Jelezko, and J. Wrachtrup, "Ultralong spin coherence time in isotopically engineered diamond," *Nature Materials 2009 8:5*, vol. 8, pp. 383–387, 4 2009.

[24] F. Jelezko and J. Wrachtrup, "Single defect centres in diamond: A review," *physica status solidi (a)*, vol. 203, pp. 3207–3225, 10 2006.

[25] G. D. Fuchs, V. V. Dobrovitski, R. Hanson, A. Batra, C. D. Weis, T. Schenkel, and D. D. Awschalom, "Excited-state spectroscopy using single spin manipulation in diamond," *Physical Review Letters*, vol. 101, p. 117601, 9 2008.

[26] R. Hanson and D. D. Awschalom, "Coherent manipulation of single spins in semiconductors," *Nature*, vol. 453, pp. 1043–1049, 6 2008.

[27] P. Neumann, R. Kolesov, V. Jacques, J. Beck, J. Tisler, A. Batalov, L. Rogers, N. B. Manson, G. Balasubramanian, F. Jelezko, and J. Wrachtrup, "Excited-state spectroscopy of single nv defects in diamond using optically detected magnetic resonance," *New Journal of Physics*, vol. 11, p. 013017, 1 2009.

[28] A. Gruber, A. Dräbenstedt, C. Tietz, L. Fleury, J. Wrachtrup, and C. V. Borczyskowski, "Scanning confocal optical microscopy and magnetic resonance on single defect centers," *Science*, vol. 276, pp. 2012–2014, 6 1997.

[29] E. Rittweger, K. Y. Han, S. E. Irvine, C. Eggeling, and S. W. Hell, "Sted microscopy reveals crystal colour centres with nanometric resolution," *Nature Photonics 2009 3:3*, vol. 3, pp. 144–147, 2 2009.

[30] D. H. Lee and J. A. Gupta, "Tunable field control over the binding energy of single dopants by a charged vacancy in gaas," *Science (New York, N.Y.)*, vol. 330, pp. 1807–1810, 12 2010.

[31] A. A. Khajetoorians, B. Chilian, J. Wiebe, S. Schuwalow, F. Lechermann, and R. Wiesendanger, "Detecting excitation and magnetization of individual dopants in a semiconductor.," *Nature*, vol. 467, pp. 1084–1087, 10 2010.

[32] D. Kitchen, A. Richardella, J. M. Tang, M. E. Flatté, and A. Yazdani, "Atom-by-atom substitution of mn in gaas and visualization of their hole-mediated interactions," *Nature 2006 442:7101*, vol. 442, pp. 436–439, 7 2006.

[33] A. Richardella, D. Kitchen, and A. Yazdani, "Mapping the wave function of transition metal acceptor states in the gaas surface," *Physical Review B - Condensed Matter and Materials Physics*, vol. 80, p. 045318, 8 2009.

[34] Y. Sainoo, H. Isshiki, S. M. F. Shahed, T. Takaoka, and T. Komeda, "Atomically resolved larmor frequency detection on si (111) -7×7 oxide surface," *Applied Physics Letters*, vol. 95, 8 2009.

[35] R. M. Feenstra, E. T. Yu, J. M. Woodall, P. D. Kirchner, C. L. Lin, and G. D. Pettit, "Cross-sectional imaging and spectroscopy of gaas doping superlattices by scanning tunneling microscopy," *Applied Physics Letters*, vol. 61, pp. 795–797, 8 1992.

[36] Z. F. Zheng, M. B. Salmeron, and E. R. Weber, "Empty state and filled state image of znga acceptor in gaas studied by scanning tunneling microscopy," *Applied Physics Letters*, vol. 64, pp. 1836–1838, 4 1994.

[37] D. Loss and D. P. DiVincenzo, "Quantum computation with quantum dots," *Physical Review A*, vol. 57, p. 120, 1 1998.

[38] B. E. Kane, "A silicon-based nuclear spin quantum computer," *Nature 1998 393:6681*, vol. 393, pp. 133–137, 5 1998.

[39] A. Imamoglu, D. D. Awschalom, G. Burkard, D. P. DiVincenzo, D. Loss, M. Sherwin, and A. Small, "Quantum information processing using quantum dot spins and cavity qed," *Physical Review Letters*, vol. 83, p. 4204, 11 1999.

[40] C. E. Pryor and M. E. Flattá, "Predicted ultrafast single qubit operations in semiconductor quantum dots," *Applied Physics Letters*, vol. 88, 11 2002.

[41] G. F. Quinteiro and C. Piermarocchi, "Entanglement and errors in the control of spins by optical coupling," *Physical Review B - Condensed Matter and Materials Physics*, vol. 72, p. 045334, 7 2005.

[42] Y. Kato, R. C. Myers, D. C. Driscoll, A. C. Gossard, J. Levy, and D. D. Awschalom, "Gigahertz electron spin manipulation using voltage-controlled g-tensor modulation," *Science*, vol. 299, pp. 1201–1204, 2 2003.

[43] Y. Kato, R. C. Myers, A. C. Gossard, and D. D. Awschalom, "Coherent spin manipulation without magnetic fields in strained semiconductors," *Nature 2004 427:6969*, vol. 427, pp. 50–53, 1 2004.

[44] D. P. DiVincenzo, D. Bacon, J. Kempe, G. Burkard, and K. B. Whaley, "Universal quantum computation with the exchange interaction," *Nature 2000 408:6810*, vol. 408, pp. 339–342, 11 2000.

[45] J. R. Petta, A. C. Johnson, J. M. Taylor, E. A. Laird, A. Yacoby, M. D. Lukin, C. M. Marcus, M. P. Hanson, and A. C. Gossard, "Applied physics: Coherent manipulation of coupled electron spins in semiconductor quantum dots," *Science*, vol. 309, pp. 2180–2184, 9 2005.

[46] M. N. Baibich, J. M. Broto, A. Fert, F. N. V. Dau, F. Petroff, P. Eitenne, G. Creuzet, A. Friederich, and J. Chazelas, "Giant magnetoresistance of (001)fe/(001)cr magnetic superlattices," *Physical Review Letters*, vol. 61, pp. 2472–2475, 11 1988.

[47] G. Binasch, P. Grünberg, F. Saurenbach, and W. Zinn, "Enhanced magnetoresistance in layered magnetic structures with antiferromagnetic interlayer exchange," *Physical Review B*, vol. 39, p. 4828, 3 1989.

[48] T. Kawahara, K. Ito, R. Takemura, and H. Ohno, "Spin-transfer torque ram technology: Review and prospect," *Microelectronics Reliability*, vol. 52, pp. 613–627, 4 2012.

[49] A. D. Kent and D. C. Worledge, "A new spin on magnetic memories," *Nature nanotechnology*, vol. 10, pp. 187–191, 3 2015.

[50] D. Apalkov, B. Dieny, and J. M. Slaughter, "Magnetoresistive random access memory: Magnetoresistive random access memory (mram) and particularly spin-transfer-torque mram is a nonvolatile memory with very high endurance and scalability. it is based on an array of magnetic tunnel junctions with magnetoresistive readout of the state of device and uses spin-transfer torque to efficiently rewrite the memory," *Proceedings of the IEEE*, vol. 104, pp. 1796–1830, 10 2016.

[51] A. V. Khvalkovskiy, D. Apalkov, S. Watts, R. Chepulskii, R. S. Beach, A. Ong, X. Tang, A. Driskill-Smith, W. H. Butler, P. B. Visscher, D. Lottis, E. Chen, V. Nikitin, and M. Krounbi, "Basic principles of stt-mram cell operation in memory arrays," *Journal of Physics D: Applied Physics*, vol. 46, p. 074001, 1 2013.

[52] B. Dieny, I. L. Prejbeanu, K. Garello, P. Gambardella, P. Freitas, R. Lehndorff, W. Raberg, U. Ebels, S. O. Demokritov, J. Akerman, A. Deac, P. Pirro, C. Adelmann, A. Anane, A. V. Chumak, A. Hirohata, S. Mangin, S. O. Valenzuela, M. C. Onbaşlı, M. d'Aquino, G. Prenat, G. Finocchio, L. Lopez-Diaz, R. Chantrell, O. Chubykalo-Fesenko, and P. Bortolotti, "Opportunities and challenges for spintronics in the microelectronics industry," *Nature Electronics 2020 3:8*, vol. 3, pp. 446–459, 8 2020.

[53] R. Vrijen, E. Yablonovitch, K. Wang, H. W. Jiang, A. Balandin, V. Roychowdhury, T. Mor, and D. DiVincenzo, "Electron-spin-resonance transistors for quantum computing in silicon-germanium heterostructures," *Physical Review A*, vol. 62, p. 012306, 6 2000.

[54] L. C. Hollenberg, A. S. Dzurak, C. Wellard, A. R. Hamilton, D. J. Reilly, G. J. Milburn, and R. G. Clark, "Charge-based quantum computing using single donors in semiconductors," *Physical Review B*, vol. 69, p. 113301, 3 2004.

[55] J. Preskill, "Reliable quantum computers," *Proceedings of the Royal Society A: Mathematical, Physical and Engineering Sciences*, vol. 454, pp. 385–410, 5 1997.

[56] P. W. Shor, "Algorithms for quantum computation: Discrete logarithms and factoring," *Proceedings - Annual IEEE Symposium on Foundations of Computer Science, FOCS*, pp. 124–134, 1994.

[57] A. Ekert and R. Jozsa, "Quantum computation and shor's factoring algorithm," *Reviews of Modern Physics*, vol. 68, p. 733, 7 1996.

[58] L. K. Grover, "Quantum mechanics helps in searching for a needle in a haystack," *Physical Review Letters*, vol. 79, p. 325, 7 1997.

[59] A. R. Calderbank and P. W. Shor, "Good quantum error-correcting codes exist," *Physical Review A*, vol. 54, p. 1098, 8 1996.

[60] A. M. Steane, "Error correcting codes in quantum theory," *Physical Review Letters*, vol. 77, p. 793, 7 1996.

[61] A. De, C. E. Pryor, and M. E. Flatté, "Electric-field control of a hydrogenic donor's spin in a semiconductor," *Physical Review Letters*, vol. 102, p. 017603, 1 2009.

[62] J. M. Tang, J. Levy, and M. E. Flatté, "All-electrical control of single ion spins in a semiconductor," *Physical Review Letters*, vol. 97, p. 106803, 9 2006.

[63] C. Gould, K. Pappert, G. Schmidt, and L. W. Molenkamp, "Magnetic anisotropies and (ga,mn)as-based spintronic devices," *Advanced Materials*, vol. 19, pp. 323–340, 2 2007.

[64] R. Fiederling, M. Keim, G. Reuscher, W. Ossau, G. Schmidt, A. Waag, L. W. Molenkamp, R. Fiederling, M. Keim, G. Reuscher, W. Ossau, G. Schmidt, A. Waag, and L. W. Molenkamp, "Injection and detection of a spin-polarized current in a light-emitting diode," *Natur*, vol. 402, pp. 787–790, 12 1999.

[65] F. Matsukura, H. Ohno, A. Shen, and Y. Sugawara, "Transport properties and origin of ferromagnetism in (ga,mn)as," *Physical Review B*, vol. 57, p. R2037, 1 1998.

[66] T. Story, R. R. Gałazka, R. B. Frankel, and P. A. Wolff, "Carrier-concentration–induced ferromagnetism in pbsnmnte," *Physical Review Letters*, vol. 56, p. 777, 2 1986.

[67] H. Ohno, H. Munekata, T. Penney, S. von Molnár, and L. L. Chang, "Magnetotransport properties of p-type (in,mn)as diluted magnetic iii-v semiconductors," *Physical Review Letters*, vol. 68, p. 2664, 4 1992.

[68] H. Ohno, A. Shen, F. Matsukura, A. Oiwa, A. Endo, S. Katsumoto, and Y. Iye, "(ga,mn)as: A new diluted magnetic semiconductor based on gaas," *Applied Physics Letters*, vol. 69, pp. 363–365, 7 1996.

[69] A. V. Esch, L. V. Bockstal, J. D. Boeck, G. Verbanck, A. S. van Steenbergen, P. J. Wellmann, B. Grietens, R. Bogaerts, F. Herlach, and G. Borghs, "Interplay between the magnetic and transport properties in the iii-v diluted magnetic semiconductor ga1xmnxas," *Physical Review B*, vol. 56, p. 13103, 11 1997.

[70] A. Haury, A. Wasiela, A. Arnoult, J. Cibert, S. Tatarenko, T. Dietl, and Y. M. d'aubigné, "Observation of a ferromagnetic transition induced by two-dimensional hole gas in modulation-doped cdmnte quantum wells," *Physical Review Letters*, vol. 79, p. 511, 7 1997.

[71] D. Ferrand, J. Cibert, A. Wasiela, C. Bourgognon, S. Tatarenko, G. Fishman, S. Koleśnik, J. Jaroszyński, T. Dietl, B. Barbara, and D. Dufeu, "Carrier induced ferromagnetic interactions and transport properties of p-zn(1-x)mnxte epilayers," *Journal of Applied Physics*, vol. 87, pp. 6451–6453, 5 2000.

[72] L. Chen, X. Yang, F. Yang, J. Zhao, J. Misuraca, P. Xiong, and S. V. Molnár, "Enhancing the curie temperature of ferromagnetic semiconductor (ga,mn)as to 200 k via nanostructure engineering," *Nano Letters*, vol. 11, pp. 2584–2589, 7 2011.

[73] T. Dietl and H. Ohno, "Dilute ferromagnetic semiconductors: Physics and spintronic structures," *Reviews of Modern Physics*, vol. 86, pp. 187–251, 3 2014.

[74] A. N. Andriotis and M. Menon, "Codoping induced enhanced ferromagnetism in diluted magnetic semiconductors," *Journal of Physics: Condensed Matter*, vol. 33, p. 393002, 7 2021.

[75] M. F. Islam and C. M. Canali, "Ab initio calculations of the magnetic properties of mn impurities on gaas (110) surfaces," *Physical Review B*, vol. 85, no. 15, p. 155306, 2012.

[76] Z. Fang and Z. Yi, "Substitutional co dopant on the gaas(110) surface: A first principles study," *Physica B: Condensed Matter*, vol. 502, pp. 1–4, 12 2016.

[77] Z. Fang and Z. Yi, "Ab-initio studies on the electronic properties of fe dopant in gaas(1 1 0) surface," *Computational Materials Science*, vol. 118, pp. 4–10, 6 2016.

[78] S. Francoeur, J. F. Klem, and A. Mascarenhas, "Optical spectroscopy of single impurity centers in semiconductors," *Physical Review Letters*, vol. 93, p. 067403, 8 2004.

[79] M. R. Deshpande, J. W. Sleight, M. A. Reed, R. G. Wheeler, and R. J. Matyi, "Spin splitting of single 0d impurity states in semiconductor heterostructure quantum wells," *Physical Review Letters*, vol. 76, p. 1328, 2 1996.

[80] R. C. Myers, M. H. Mikkelsen, J. M. Tang, A. C. Gossard, M. E. Flatté, and D. D. Awschalom, "Zero-field optical manipulation of magnetic ions in semiconductors," *Nature Materials 2008 7:3*, vol. 7, pp. 203–208, 2 2008.

[81] T. Schlesinger, "Gallium arsenide," *Encyclopedia of Materials: Science and Technology*, pp. 3431–3435, 1 2001.

[82] J. G. Lee, *Computational Materials Science: An Introduction*. Boca Raton, FL: CRC Press, Taylor & Francis Group, second ed., 2017. Includes bibliographical references and index.

[83] F. Giustino, *Materials Modelling Using Density Functional Theory: Properties and Predictions*. Oxford, United Kingdom: Oxford University Press, 2014. First edition, includes bibliographical references and index.

[84] R. M. Martin, *Electronic Structure: Basic Theory and Practical Methods*. Cambridge, United Kingdom: Cambridge University Press, 2020. Includes bibliographical references and index.

[85] P. Hohenberg and W. Kohn, "Inhomogeneous electron gas," *Physical Review*, vol. 136, p. B864, 11 1964.

[86] W. Kohn and L. J. Sham, "Self-consistent equations including exchange and correlation effects," *Physical Review*, vol. 140, p. A1133, 11 1965.

[87] U. V. Barth and L. Hedin, "A local exchange-correlation potential for the spin polarized case. i," *Journal of Physics C: Solid State Physics*, vol. 5, p. 1629, 7 1972.

[88] A. K. Rajagopal and J. Callaway, "Inhomogeneous electron gas," *Physical Review B*, vol. 7, p. 1912, 3 1973.

[89] D. M. Ceperley and B. J. Alder, "Ground state of the electron gas by a stochastic method," *Physical Review Letters*, vol. 45, p. 566, 8 1980.

[90] J. P. Perdew and A. Zunger, "Self-interaction correction to density-functional approximations for many-electron systems," *Physical Review B*, vol. 23, p. 5048, 5 1981.

[91] E. Runge and E. K. Gross, "Density-functional theory for time-dependent systems," *Physical Review Letters*, vol. 52, p. 997, 3 1984.

[92] N. A. Spaldin, *Magnetic Materials*. Cambridge University Press, 2nd ed., 2010.

[93] W. Pauli, "Über den zusammenhang des abschlusses der elektronengruppen im atom mit der komplexstruktur der spektren," *Zeitschrift für Physik*, vol. 31, 1925.

[94] W. J. Mullin and G. Blaylock, "Quantum statistics: Is there an effective fermion repulsion or boson attraction?," *American Journal of Physics*, vol. 71, pp. 1223–1231, November 11 2003.

[95] D. J. Griffiths, *Introduction to Quantum mechanics*. Pearson Education, 2nd ed., 2005.

[96] S. Blundell, *Magnetism in Condensed Matter*. Oxford University Press, 2001.

[97] W. Heisenberg, "Zur theorie des ferromagnetismus," *Zeitschrift für Physik*, vol. 49, no. 9, pp. 619–636, 1928.

[98] P. Giannozzi, S. Baroni, N. Bonini, M. Calandra, R. Car, C. Cavazzoni, D. Ceresoli, G. L. Chiarotti, M. Cococcioni, I. Dabo, A. D. Corso, S. D. Gironcoli, S. Fabris, G. Fratesi, R. Gebauer, U. Gerstmann, C. Gougoussis, A. Kokalj, M. Lazzeri, L. Martin-Samos, N. Marzari, F. Mauri, R. Mazzarello, S. Paolini, A. Pasquarello, L. Paulatto, C. Sbraccia, S. Scandolo, G. Sclauzero, A. P. Seitsonen, A. Smogunov, P. Umari, and R. M. Wentzcovitch, "Quantum espresso: a modular and open-source software project for quantum simulations of materials," *Journal of physics. Condensed matter : an Institute of Physics journal*, vol. 21, 2009.

[99] P. Giannozzi, O. Andreussi, T. Brumme, O. Bunau, M. B. Nardelli, M. Calandra, R. Car, C. Cavazzoni, D. Ceresoli, M. Cococcioni, N. Colonna, I. Carnimeo, A. D. Corso, S. D. Gironcoli, P. Delugas, R. A. Distasio, A. Ferretti, A. Floris, G. Fratesi, G. Fugallo, R. Gebauer, U. Gerstmann, F. Giustino, T. Gorni, J. Jia, M. Kawamura, H. Y. Ko, A. Kokalj, E. Kücükbenli, M. Lazzeri, M. Marsili, N. Marzari, F. Mauri, N. L. Nguyen, H. V. Nguyen, A. Otero-De-La-Roza, L. Paulatto, S. Poncé, D. Rocca, R. Sabatini, B. Santra, M. Schlipf, A. P. Seitsonen, A. Smogunov, I. Timrov, T. Thonhauser, P. Umari, N. Vast, X. Wu, and S. Baroni, "Advanced capabilities for materials modelling with quantum espresso," *Journal of physics. Condensed matter : an Institute of Physics journal*, vol. 29, 10 2017.

[100] P. Giannozzi, O. Baseggio, P. Bonfà, D. Brunato, R. Car, I. Carnimeo, C. Cavazzoni, S. D. Gironcoli, P. Delugas, F. F. Ruffino, A. Ferretti,

N. Marzari, I. Timrov, A. Urru, and S. Baroni, "Quantum espresso toward the exascale," *The Journal of chemical physics*, vol. 152, 4 2020.

[101] Z. Yi, Y. Ma, and M. Rohlfing, "Silicon donors at the gaas(110) surface: A first principles study," *Journal of Physical Chemistry C*, vol. 115, pp. 23455–23462, 12 2011.

[102] S. Y. Tong, A. R. Lubinsky, B. J. Mrstik, and M. A. V. Hove, "Surface bond angle and bond lengths of rearranged as and ga atoms on gaas(110)," *Physical Review B*, vol. 17, pp. 3303–3309, 1978.

[103] G. Binnig, H. Rohrer, C. Gerber, and E. Weibel, "Tunneling through a controllable vacuum gap," *Applied Physics Letters*, vol. 40, pp. 178–180, 1 1982.

[104] G. Binning, H. Rohrer, C. Gerber, and E. Weibel, "Surface studies by scanning tunneling microscopy," *Physical Review Letters*, vol. 49, pp. 57–61, 1982.

[105] C. J. Chen, *Introduction to Scanning Tunneling Microscopy*. Oxford University Press, 2nd ed., 2007.

[106] J. Tersoff and D. R. Hamann, "Theory of the scanning tunneling microscope," *Physical Review B*, vol. 31, pp. 805–813, 1985.

Appendix A

Relaxation results for Cr, Co, and V Dimers

	FM-Far	AFM-Far	FM-Near	AFM-Near
d	5.6874	5.6871	4.1162	4.0580
d_1	2.3924	2.3954	2.3356	2.3955
d_2	2.3758	2.3783	2.3923	2.3924
d_3	2.3937	2.3939	2.3178	2.3808
d_4	2.3927	2.3930	2.3178	2.3808
d_5	2.3758	2.3787	2.3923	2.3925
d_6	2.3924	2.3944	2.3356	2.3955

Table A.1: Tabulated values for Cr relaxed positions in FM and AFM configurations in Å (Far and Near).

	FM-Far	AFM-Far	FM-Near	AFM-Near
d	5.6874	5.6874	3.9191	3.9193
d_1	2.2093	2.2093	2.1743	2.1743
d_2	2.1950	2.1966	2.2148	2.2149
d_3	2.2093	2.2093	2.1680	2.1683
d_4	2.2093	2.2092	2.1680	2.1683
d_5	2.1950	2.1965	2.2148	2.2149
d_6	2.2093	2.2092	2.1742	2.1743

Table A.2: Tabulated values for Co relaxed positions in FM and AFM configurations in Å (Far and Near).

	FM-Far	AFM-Far	FM-Near	AFM-Near
d	5.6874	5.6874	4.0470	4.1049
d_1	2.2358	2.3585	2.3657	2.3549
d_2	2.4106	2.4120	2.4085	2.4093
d_3	2.2358	2.3574	2.3540	2.3646
d_4	2.3558	2.3574	2.3540	2.3645
d_5	2.4107	2.4120	2.4085	2.4093
d_6	2.3568	2.3585	2.3657	2.3548

Table A.3: Tabulated values for V relaxed positions in FM and AFM configurations in Å (Far and Near).

Appendix B

DOS and PDOS Results

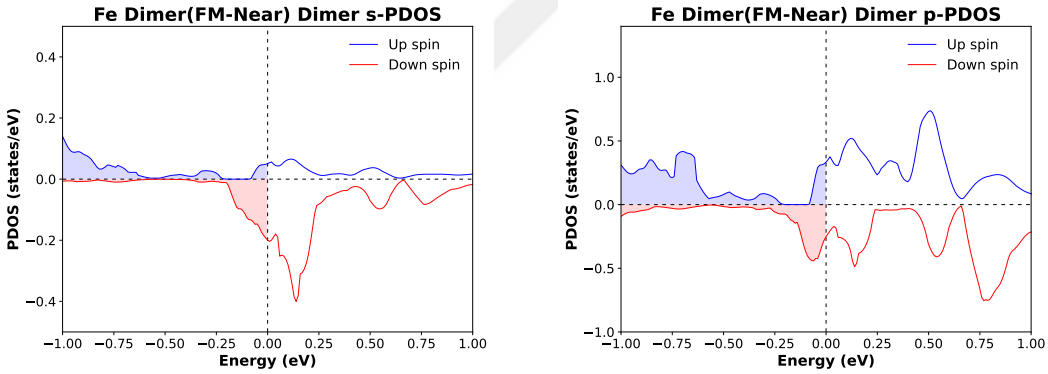

(a) (b)

Figure B.1: s and p PDOS results for Fe dimers on near ferromagnetic configuration.

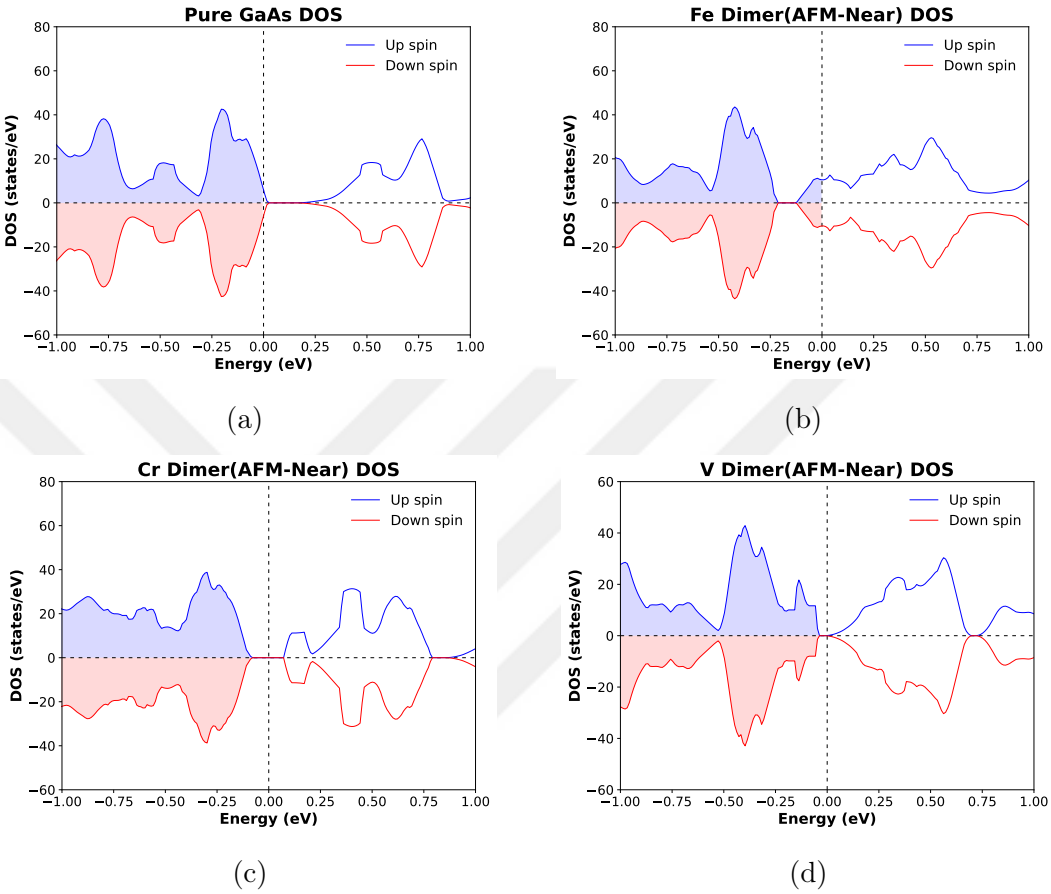

Figure B.2: DOS results for 112 atoms GaAs(110) surface. (a) pure GaAs configuration. (b) Fe dimer antiferroamagnetic near configuration. (c), and (d) Cr and V dimer antiferromagnetic near configurations respectively. Figures demonstrate the in-gap states and magnetic behavior around the Fermi level (dashed line).

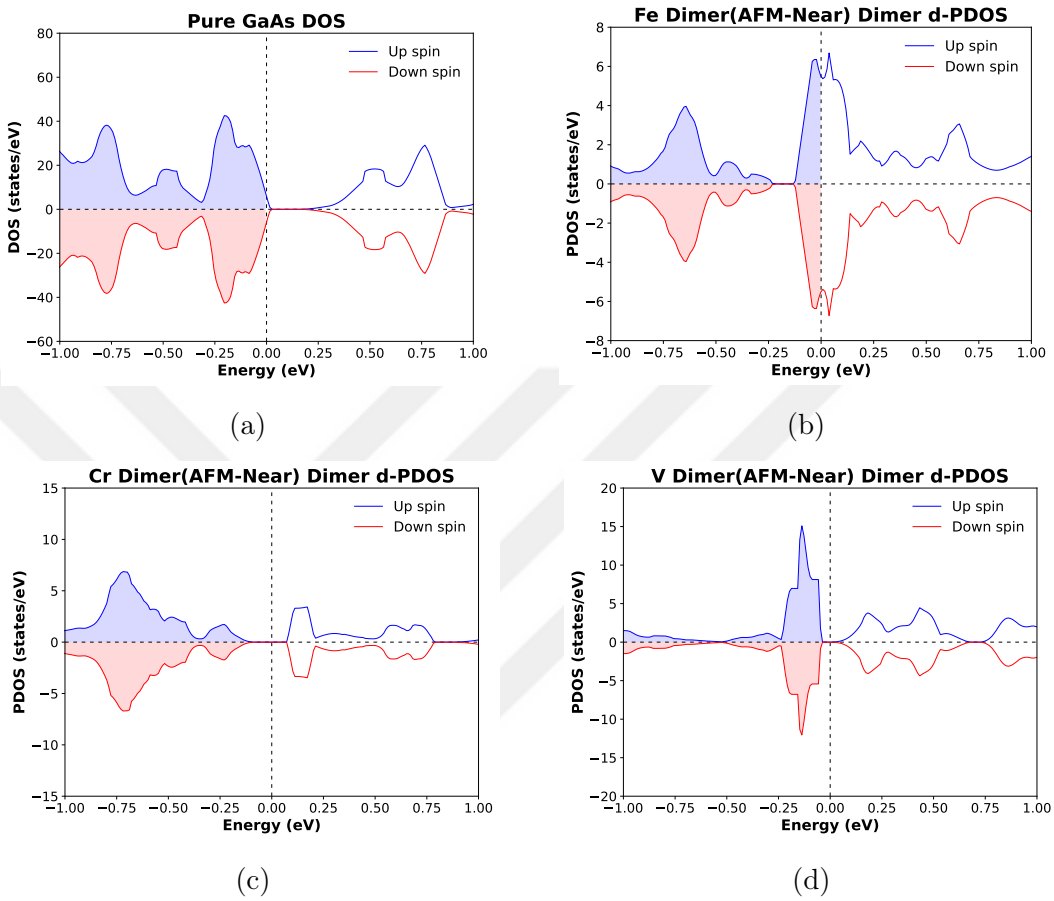

Figure B.3: Pure GaAs(110) and dimers' d-PDOS projections for near ferromagnetic configuration. (a) Pure GaAs(110). (b) Fe dimer' d-PDOS. (c) for Cr and (d) for V dimer d-PDOS on antiferromagnetic near configuration. Fermi level (dashed line).

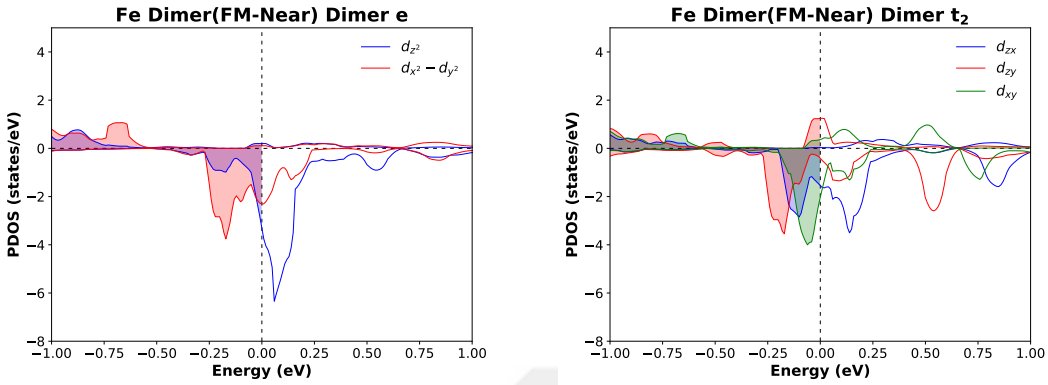

(a) (b)

Figure B.4: (a) e and (b) t_2 projections for Fe dimer on ferromagnetic near configuration.

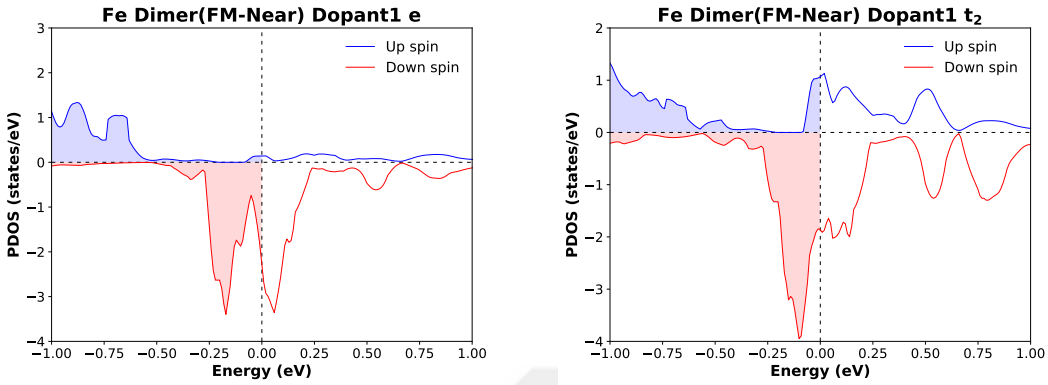

(a) (b)

Figure B.5: Spin polarization and in-gap sates on (a), e and (b), t_2 projections.

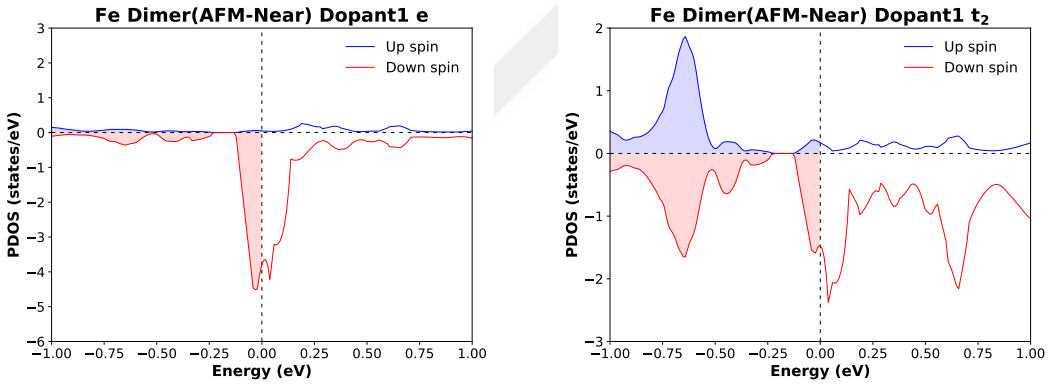

(a) (b)

Figure B.6: Spin polarization and in-gap sates on d-PDOS projections for anti-ferromagnetic aligned near configuration. (a) for dopant 1 e projection and (b) for dopant 2 t_2 projection.

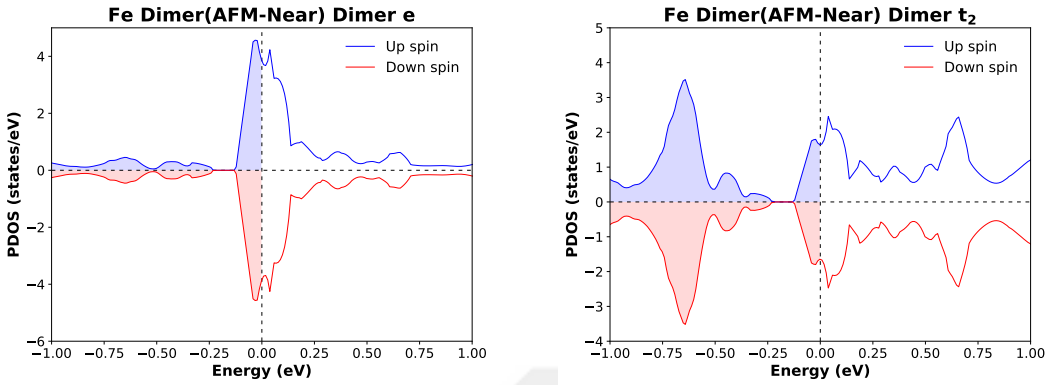

(a) (b)

Figure B.7: Spin polarization and in-gap sates of dimers on (a) e and (b) t_2 projections for antiferromagnetic near configuration.